# cmgh

ORIGINAL RESEARCH

SMN Depleted Mice Offer a Robust and Rapid Onset Model of Nonalcoholic Fatty Liver Disease

Marc-Olivier Deguise,[1,2,3] Chantal Pileggi,[4] Yves De Repentigny,[1] Ariane Beauvais,[1] Alexandra Tierney,[1] Lucia Chehade,[1,2,3] Jean Michaud,[5] Maica Llavero-Hurtado,[6,7] Douglas Lamont,[8] Abdelmadjid Atrih,[8] Thomas M. Wishart,[6,7] Thomas H. Gillingwater,[6,9] Bernard L. Schneider,[10,11] Mary-Ellen Harper,[4] Simon H. Parson,[6,12] and Rashmi Kothary[1,2,3,13]

[1]Regenerative Medicine Program, Ottawa Hospital Research Institute, Ottawa, Ontario, Canada; [2]Department of Cellular and Molecular Medicine, University of Ottawa, Ottawa, Ontario, Canada; [3]Centre for Neuromuscular Disease, University of Ottawa, Ottawa, Ontario, Canada; [4]Department of Biochemistry, Microbiology and Immunology, Ottawa Institute of Systems Biology, University of Ottawa, Ottawa, Ontario, Canada; [5]Department of Pathology and Laboratory Medicine, Faculty of Medicine, University of Ottawa, Ottawa, Ontario, Canada; [6]Euan MacDonald Centre for Motor Neurone Disease Research, University of Edinburgh, Edinburgh, United Kingdom; [7]The Roslin Institute, Royal (Dick) School of Veterinary Studies, College of Medicine and Veterinary Medicine, University of Edinburgh, Edinburgh, United Kingdom; [8]FingerPrints Proteomics Facility, University of Dundee, Dundee, United Kingdom; [9]College of Medicine & Veterinary Medicine, University of Edinburgh, Edinburgh, United Kingdom; [10]Brain Mind Institute, Ecole Polytechnique Fédérale de Lausanne (EPFL), Lausanne, Switzerland; [11]Bertarelli Foundation Gene Therapy Platform, School of Life Sciences, Ecole Polytechnique Fédérale de Lausanne (EPFL), Geneva, Switzerland; [12]Institute of Medical Sciences, University of Aberdeen, Aberdeen, United Kingdom; and [13]Department of Medicine, University of Ottawa, Ottawa, Ontario, Canada
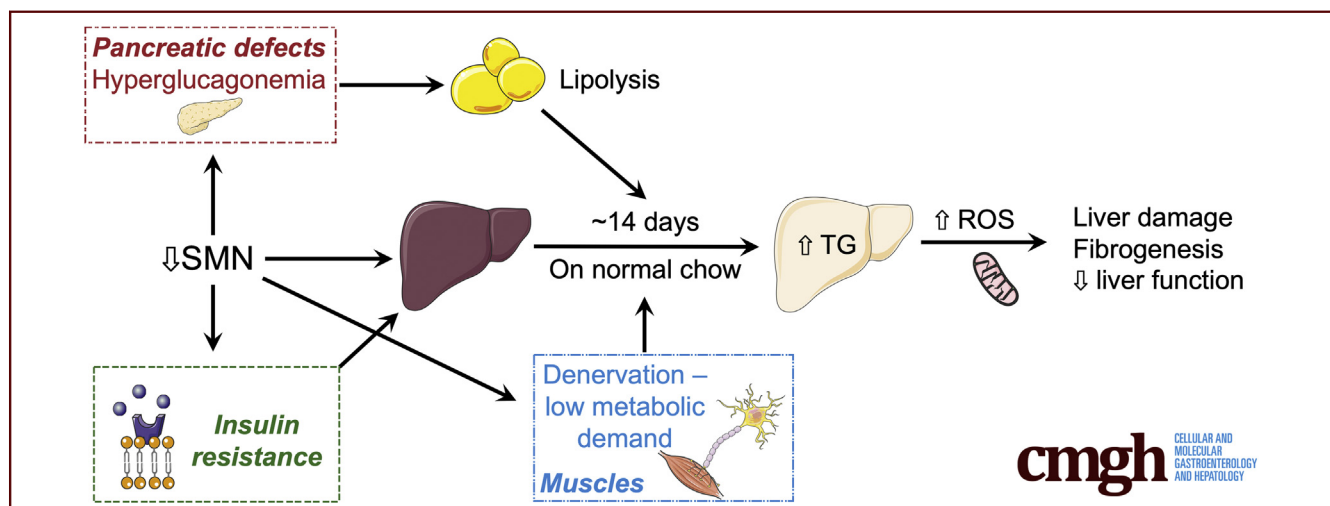
SUMMARY

The $Smn^{2B/-}$ mice, a mouse model with reduced level of SMN protein, represent a good model of microvesicular steatohepatitis. They offer a reliable, low-cost, early-onset model to identify molecular players in the pathogenesis of NAFLD in both the adult and pediatric populations.

BACKGROUND & AIMS: Nonalcoholic fatty liver disease (NAFLD) is considered a health epidemic with potential devastating effects on the patients and the healthcare systems. Current preclinical models of NAFLD are invariably imperfect and generally take a long time to develop. A mouse model of survival motor neuron (SMN) depletion ($Smn^{2B/-}$ mice) was recently shown to develop significant hepatic steatosis in less than 2 weeks from birth. The rapid onset of fatty liver in $Smn^{2B/-}$ mice provides an opportunity to identify molecular markers of NAFLD. Here, we investigated whether $Smn^{2B/-}$ mice display typical features of NAFLD/nonalcoholic steatohepatitis (NASH).

METHODS: Biochemical, histologic, electron microscopy, proteomic, and high-resolution respirometry were used.

RESULTS: The $Smn^{2B/-}$ mice develop microvesicular steatohepatitis within 2 weeks, a feature prevented by AAV9-SMN gene therapy. Although fibrosis is not overtly apparent in histologic sections of the liver, there is molecular evidence of fibrogenesis and presence of stellate cell activation. The consequent liver damage arises from mitochondrial reactive oxygen species production and results in hepatic dysfunction in protein output, complement, coagulation, iron homeostasis, and insulin-like

growth factor-1 metabolism. The NAFLD phenotype is likely due to non-esterified fatty acid overload from peripheral lipolysis subsequent to hyperglucagonemia compounded by reduced muscle use and insulin resistance. Despite the low hepatic mitochondrial content, isolated mitochondria show enhanced β-oxidation, likely as a compensatory response, resulting in the production of reactive oxygen species. In contrast to typical NAFLD/NASH, the $Smn^{2B/-}$ mice lose weight because of their associated neurological condition (spinal muscular atrophy) and develop hypoglycemia.

CONCLUSIONS: The $Smn^{2B/-}$ mice represent a good model of microvesicular steatohepatitis. Like other models, it is not representative of the complete NAFLD/NASH spectrum. Nevertheless, it offers a reliable, low-cost, early-onset model that is not dependent on diet to identify molecular players in NAFLD pathogenesis and can serve as one of the very few models of microvesicular steatohepatitis for both adult and pediatric populations. *(Cell Mol Gastroenterol Hepatol 2021;12:354–377; https://doi.org/10.1016/j.jcmgh.2021.01.019)*

N onalcoholic fatty liver disease (NAFLD) is a significant burden on population health. At this time, it is estimated to affect the lives of nearly 1 billion individuals worldwide.[1] As many as 33% of Americans and 10% of children are thought to have the condition.[1,2] NAFLD is often associated with other ailments including insulin resistance and type 2 diabetes mellitus (T2DM), visceral obesity, hypertension, as well as dyslipidemia (often referred to as the metabolic syndrome), leading to compounding comorbidities. Indeed, NALFD is associated with shortened survival.[3,4] Among NAFLD patients, "liver disease" is the third most common cause of death (13%) in comparison with the general population, where it sits at the 13th position and accounts for less than 1% of deaths.[3,4]

NAFLD is characterized by increased storage of fatty acids in more than 5% of hepatocytes in the absence of alcohol use.[1,5] It presents as a spectrum of severity that encompasses simple steatosis, steatohepatitis, cirrhosis, and hepatocellular carcinoma.[6] Simple steatosis, which is the accumulation of hepatic fat with minimal consequences, is most commonly seen. However, a proportion of NAFLD patients will go on to develop inflammation of the liver, termed *steatohepatitis* or *nonalcoholic steatohepatitis* (NASH), which can be complicated by fibrosis, cirrhosis, and ultimately hepatocellular carcinoma.[3,7] Despite NAFLD evolving as a major life-impairing entity, effective pharmacologic options to treat the disease are sparse.[8] This is in part due to the complex nature of NAFLD pathogenesis, which may involve multiple organ systems, including peripheral adipose tissue, the gut, and potentially other metabolic organs.[6,9] Although simple steatosis appears to be a consequence of an imbalance of fatty acid input (lipogenesis, import) and output (fatty acid oxidation, export) in the liver,[10] it is currently hypothesized that "multiple hits" are required to develop NASH and more severe phenotypes.[6]

Multiple mouse models of NAFLD exist and offer great insight into molecular signaling events. However, in the context of the NAFLD research landscape, these models remain invariably imperfect in modelling the true phenotype of patients with NAFLD/NASH.[6,10–12] Most mouse models do not typically display all the stages of NAFLD (simple steatosis, NASH, cirrhosis, hepatocellular carcinoma). Furthermore, there are many dietary models that hope to replicate the humanistic dietary components inducing associated conditions such as obesity, T2DM, and NAFLD. Unfortunately, the dietary approach generally necessitates months for the development of the desired phenotype, with consequent high cost of the food required, colony maintenance, space, and experimental interventions, leading to low cost-effectiveness of these models. For example, the Western-style diet (or fast food diet) can take as much as 6 months to lead to the development of NASH.[9,13] On the other hand, the methionine- and choline-deficient diet (MCD) leads to a much faster NASH phenotype (∼ 2–8 weeks), yet the pathogenic mechanisms lack the systemic features of the human presentation marked by metabolic syndrome.[14,15] Monogenic models have also found a place in the NAFLD arena. The *ob/ob* and *db/db* mouse models lead to leptin pathway disruption with subsequent hyperphagia, obesity, diabetes, and steatosis.[6] However, they lack the inflammatory process and progression to NASH unless a second insult occurs.[6,16] Moreover, single gene models are considered a reductionist approach to the pathogenesis of NAFLD.[9] Although these represent only a few examples of all available models, very few, if any, offer a rapid onset of NAFLD/NASH, which would allow for efficient identification of molecular targets and testing of therapeutic strategies.

The $Smn^{2B/-}$ mouse model was initially created to model a neurological condition called spinal muscular atrophy (SMA). It contains a 3 base pair substitution in the *survival motor neuron* (*Smn*) gene, leading to alternative splicing of exon 7,[17] while the other allele is a knockout allele. The Smn^{2B} allele leads to a rapidly degraded truncated Smn

Most current article

protein in the majority of the cases, whereas full-length Smn protein production occurs about 15% of the time.[17–19] The SMN protein was first identified to play a key role in pre-mRNA splicing.[20–22] SMN is also involved in a number of additional key cellular pathways, most pertaining to RNA metabolism.[21,23] As such, SMN depletion has far-reaching effects on the transcriptome and cellular functions in all cell types of the body. Phenotypically, the $Smn^{2B/-}$ mouse model shows loss of motor neurons, neuromuscular junction abnormalities, skeletal muscle atrophy, muscle weakness, weight loss, and a shortened lifespan of 25 days.[18] In addition, within the span of 2 weeks after birth, the $Smn^{2B/-}$ mouse displayed rapid onset of fatty liver disease and dyslipidemia while exposed to a normal chow diet.[24] $Smn^{2B/-}$ mice could offer a new model of NAFLD/NASH with a rapid disease onset without the need of long-term diet regimen for new molecular insights in NAFLD/NASH pathogenesis.

In a comprehensive analysis of the metabolic defects in $Smn^{2B/-}$ mice, we here show development of NAFLD and more specifically steatohepatitis with molecular evidence of induction of a fibrogenic process without established fibrosis in a very short time span (less than 2 weeks).[24] NAFLD in $Smn^{2B/-}$ mice was prevented by adeno-associated virus 9 (AAV9)-SMN mediated gene therapy. Ultimately, the metabolic defects in $Smn^{2B/-}$ mice lead to significant functional impairment in general protein production, complement protein expression, coagulation protein expression, and insulin-like growth factor 1 (IGF-1) and iron homeostasis pathway regulation. The emergence of the NAFLD phenotype in $Smn^{2B/-}$ mice is likely from a dysfunctional pancreas-liver axis, insulin resistance, intrinsic hepatocyte defects, and reduced muscle use caused by denervation. Despite showing many features of NAFLD, the $Smn^{2B/-}$ mice do not develop obesity, hyperinsulinemic hyperglycemia, or hepatic fibrosis. Altogether, the $Smn^{2B/-}$ mice will serve as one of the very few models of microvesicular steatohepatitis for both adult and pediatric populations. Like other models, the $Smn^{2B/-}$ mice are not representative of the complete NAFLD/NASH spectrum and features. Nevertheless, $Smn^{2B/-}$ mice offer a reliable, low-cost model to identify molecular players in the pathogenesis of NAFLD.

Results

Smn[2B/-] Mice Develop Steatohepatitis With Molecular Evidence of Induction of the Fibrogenic Process

We have previously identified microvesicular steatosis and dyslipidemia (elevated total cholesterol, very low density lipoprotein [VLDL], low-density lipoprotein [LDL], and reduced high-density lipoprotein [HDL]) in $Smn^{2B/-}$ mice, occurring in the span of a few days, typically between postnatal day (P) 9 and P13.[24] Here we show that the microvesicular steatosis in $Smn^{2B/-}$ mice is directly due to Smn depletion because it can be completely prevented by gene therapy using intravenous injection of the scAAV9-CB-SMN vector (Figure 1A–D). It is important to note that levels of triglycerides and cholesterol esters were also restored to normal levels in the livers of treated $Smn^{2B/-}$ mice (Figure 1E and F). Next, we sought to investigate the severity, functional consequences, and mechanisms underpinning NAFLD in these mice. Plasma levels of serum transaminases alanine aminotransferase (ALT) and aspartate aminotransferase (AST), markers of liver damage, were mildly elevated in P19 $Smn^{2B/-}$ mice (Figure 1G and H). Muscular dystrophy patients can exhibit elevated serum transaminase levels, making skeletal muscle a potential source.[25] However, muscles from $Smn^{2B/-}$ mice are not degenerating,[26] eliminating the possibility that they could be a source of transaminase. Plasma alkaline phosphatase (ALP) remained normal, but hepatic ALP staining was enhanced in livers from symptomatic $Smn^{2B/-}$ mice (data not shown). An active apoptotic process is apparent as indicated by increased transcript levels for multiple cell death genes such as Fas receptor (FasR), tumor necrosis factor receptor superfamily member 1A (TNFR1), BCL2 associated X protein (Bax), and tumor protein p53 (p53) (Figure 1I), together with increased caspase 3 staining in livers of P17–19 $Smn^{2B/-}$ mice (Figure 1K and L). The hepatic apoptosis appears to be p53-dependent, because expression of classical targets of p53,[27] cyclin dependent kinase inhibitor 1A (p21), and Mdm2, were strongly up-regulated (Figure 1J). We next performed a polymerase chain reaction gene array aimed to determine whether a fibrogenic process was active in $Smn^{2B/-}$ mice. We found that 36 of the 84 genes contained in the array showed 1.5-fold or greater change compared with wild-type (WT) (29 up-regulated, 7 down-regulated) (Figure 1M). Among the perturbed genes included those involved in the pro-fibrotic process, genes encoding extracellular matrix (ECM) cell adhesion molecules, ECM remodeling enzymes, and transforming growth factor β superfamily members (Figure 1N). Of note, the induction of platelet-derived growth factor (pdgfa and pdgfb), a change in ECM composition, and expression of integrins (itga2, itga3, itgb3, itgb8) are all signs of initiation of hepatic stellate cell activation, which would lead to fibrogenesis.[28] Moreover, the expressions of transforming growth factor beta 2 (tgfbr2) and connective tissue growth factor (ctgf) are also considered strong fibrogenic stimuli.[28] Smooth muscle actin (acta2) was increased 2-fold, which can be indicative of activated hepatic stellate cells.[29] The strong induction of tissue inhibitor of metalloproteinase (Timp1) suggests an inhibition of endogenous ECM breakdown enzymes, which will likely exacerbate fibrosis.[28] Indeed, we observed the presence of enhanced alpha smooth muscle actin positive cells in the liver parenchyma of P19 $Smn^{2B/-}$ mice, indicating stellate cell activation (Figure 1O and P). We observed no hepatic neutrophil infiltration because neutrophils were mostly present in blood vessels rather than in the liver (data not shown). Finally, P17–19 $Smn^{2B/-}$ mice did not display overt increase in collagen deposition (Figure 1Q–T). Overall, our analysis shows that $Smn^{2B/-}$ mice have steatohepatitis, hepatic cell death, and underlying molecular changes indicative of potential fibrogenesis, but without overt collagen deposition, perhaps because of the shortened lifespan of these mice.
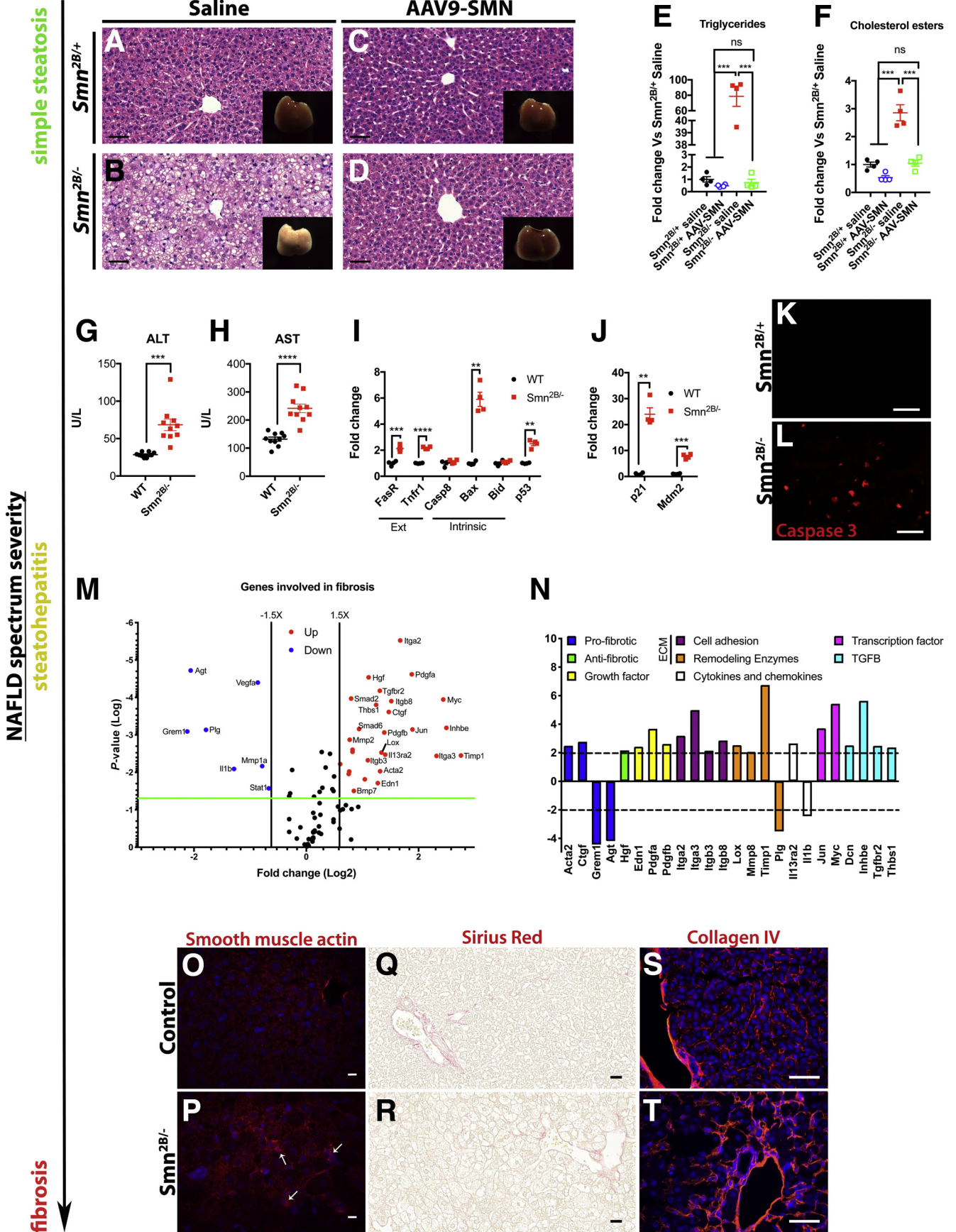
NAFLD in Smn$^{2B/-}$ Mice Leads to Impairment of Hepatic Function

We next sought to identify whether liver damage in SMN depleted mice translated into functional sequelae by using important and translatable clinical readouts. Total protein and albumin were reduced in the plasma of P19 Smn$^{2B/-}$ mice (Figure 2A and B). We identified significant reduction in expression of many complement genes (Figure 2C) and altered transcript levels of genes involved in hemostasis in the liver of SMN depleted mice (Figure 2D). We also found transcripts for hepatic nuclear factor 4 alpha (HNF4a), a transcription factor mediating synthetic capacity of the liver, to be reduced in Smn$^{2B/-}$ mice in a similar fashion to those with severe liver disease[30,31] (Figure 2D). There was no difference in megakaryocyte or platelet number when staining for CD41 (data not shown).

Iron metabolism and NAFLD have been suggested to be associated.[32] We also identified many dysregulated transcripts for genes involved in iron metabolism, including *hepcidin*, a gene producing hepcidin protein that acts as a master regulator of iron levels,[33] as well as *transferrin*, *heme oxygenase 1*, and *ceruloplasmin* (Figure 2E). Accompanying these were concordant changes in protein levels of hepcidin and heme oxygenase but not transferrin (Figure 2F). Hepcidin was further shown to be decreased by immunohistochemistry (Figure 2G and H). Plasma iron levels trended lower (Figure 2I), but hepatic stores appeared unaffected in Smn$^{2B/-}$ animals (Figure 2J and K). We observed a trend toward higher levels of total bilirubin in the plasma of Smn$^{2B/-}$ mice (Figure 2L). This is likely due to the reduced efficacy of the hepatocytes to process bilirubin rather than blockage along the biliary tree. To test whether the molecular changes may affect iron dynamics and storage, the Smn$^{2B/-}$ mice were injected with iron dextran to observe uptake. Iron accumulation was more severe in the Smn$^{2B/-}$ livers upon iron loading, despite some variability seen in the Smn$^{2B/-}$ livers likely because of injection efficacy (Figure 2M–U). This is in line with reduced hepcidin expression, because hepcidin inhibits iron absorption in the gastrointestinal tract.[33] Our results are consistent with previous work showing that iron metabolism is affected by Smn depletion.[34,35]

The liver is also a key source of growth factors, including IGF1. We identified an important reduction in *Igf1* and insulin-like growth factor binding protein acid labile subunit (*Igfals*) transcript levels and an up-regulation of insulin-like growth factor 1 receptor (*Igf1r*) and insulin-like growth factor binding protein 1 (*Igfbp1*) transcript levels (Figure 2V). A remarkable and progressive reduction of plasma IGF1 protein was observed over time in Smn$^{2B/-}$ mice (Figure 2W). These data are consistent with previous reports in other SMN depleted mouse models[36–38] and possibly NAFLD.[39] To test whether restoration of IGF1 in Smn$^{2B/-}$ mice would attenuate the liver pathology, we performed intravenous injection of AAV9-hIGF1 at P1. However, we did not see any changes at the level of the hepatic triglyceride content in AAV9-hIGF1 treated mice (data not shown). The level of endogenous mouse IGF1 was also not improved, and human IGF1 was undetectable in the plasma (data not shown).

Identification of Molecular Mechanisms Underpinning NAFLD in Smn$^{2B/-}$ Mice

To identify alterations in specific molecular pathways that could render SMN depleted liver more susceptible to NAFLD, we undertook tandem mass tagging (TMT) proteomic analysis of livers from presymptomatic P0 and P2 Smn$^{2B/-}$ mice compared with WT, specifically to look for molecular changes present well before any overt pathology. We compartmentalized the data into biologically relevant subgroups that are based on the timing of altered protein abundance detection. This produced 4 subgroups, A, B, C, and NS, where proteins in subgroup A (14% of the total IDs) represent those whose expression is already significantly altered at P0 but revert to WT basal levels at P2. Subgroup NS (not altered at either P0 or P2) contained 65% of IDs (Figure 3A). We concluded that the proteins in these subgroups (A and NS) were therefore unlikely to be important for the NAFLD phenotype in the Smn$^{2B/-}$ mice. Conversely, proteins in subgroup B (unchanged at P0, but significantly changed at P2) included 11% of total proteins, and subgroup C (altered at both P0 and P2) including 10% of total proteins were of more interest. Analysis of subgroup B using

---

Figure 1. (See previous page). Symptomatic Smn$^{2B/-}$ mice suffer from significant liver damage without fibrosis. (A–D) Microvesicular steatosis is evident (original magnification, ×40; H&E staining) at P19 effectively prevented by systemic AAV9-SMN injection at P1. (E and F) Levels of triglycerides and cholesterol esters were restored to normal levels in the liver of AAV9-SMN treated Smn$^{2B/-}$ mice. (G and H) Elevation of ALT and AST in plasma of Smn$^{2B/-}$ mice at P19. (H–J) FasR, TNFR1, Bax, p53, as well as p53 transcriptional targets p21 and Mdm2 transcripts were significantly increased in the liver. (K and L) Increased caspase 3 staining in P17 Smn$^{2B/-}$ livers (original magnification, ×100). (M) PCR array targeting fibrosis pathways revealed 36 of 84 genes to be significantly changed 1.5-fold or greater in Smn$^{2B/-}$ livers. *Green horizontal line* represents threshold for $P = .05$, and *vertical lines* represent a change of 1.5-fold. (N) Genes with more than 2-fold change were found in multiple categories of the fibrosis pathways. (O and P) Smooth muscle actin staining (original magnification, ×63) in the liver parenchyma in accordance with stellate cell activation (*arrows*) in Smn$^{2B/-}$ livers at P19. (Q–T) Representative images of Sirius red (original magnification, ×40) and collagen IV (original magnification, ×200) staining show no overt difference in hepatic fibrosis in P17–19 Smn$^{2B/-}$ mice. QPCR data were normalized with SDHA and PolJ (I and J). Scale bar represents (O and P) 10 μm, (Q and R) 20 μm, (A–D) 50 μm, and (K, L, S, and T) 100 μm. N value for each experiment is as follows: N = 10 for G and H; 4 for A–F, I, J, M, N; 3–4 for K and L; 3 for O and P; 5 for Q and R; and 4 for S and T. Statistical analysis were one-way ANOVA with Tukey multiple comparison test for E and F and unpaired two-sided Student t test for G–J. P values from PCR array were obtained from the Qiagen analysis platform. *$P \leq .05$, **$P \leq .01$, ***$P \leq .001$, and ****$P \leq .0001$.

BioLayout *Express 3D* and Database for Annotation, Visualization and Integrated Discovery (DAVID) identified the mitochondrion cluster (increased protein expression) and the lipid metabolism cluster (decreased protein expression) (Figure 3*B*). A similar analysis of subgroup C identified clusters again associated with mitochondria (proteins significantly up-regulated at both P0 and P2), extracellular signaling (proteins significantly decreased at both P0 and P2), and ECM proteins (significantly decreased at P0, however significantly increased at P2) (Figure 3*C*). To further refine potential pathways involved, we used ingenuity pathway analysis (IPA) software on proteins within
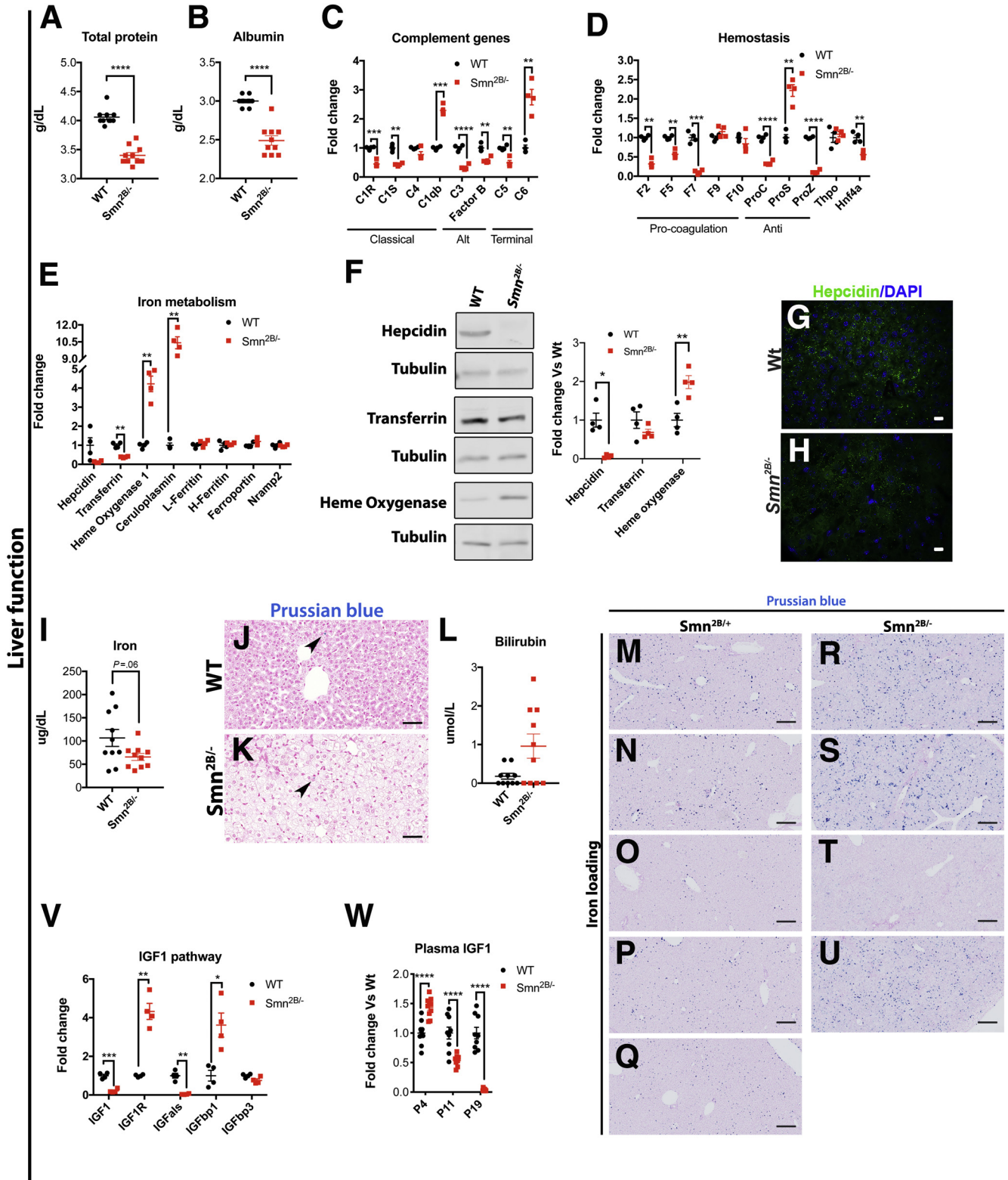
subgroups B (Figure 3D and E) and C (Figure 3F). Of interest, the results from subgroup C revealed alterations in pathways related to oxidative phosphorylation ($P = 6.35 \times 10^{-3}$) and mitochondrial dysfunction ($P = 1.11 \times 10^{-2}$) (Figure 3F). Furthermore, IPA analysis identified metabolism ($P = 3.53 \times 10^{-12}$) and homeostasis of lipids ($P = 1.68 \times 10^{-9}$) as some of the top functional subgroupings perturbed in $Smn^{2B/-}$ liver at P0 (Figure 3G). Thus, this proteomic screen points toward mitochondrial dysfunction, a critical player in fatty acid clearance through β-oxidation.

Assessment of Mitochondrial Number, Anatomy, and Function in Livers of Smn²B/- Mice

Because of the proteomic data findings and the possibility that impaired mitochondrial function could be driving NAFLD/NASH in $Smn^{2B/-}$ mice, we focused on mitochondrial content, structure, and function. Oxidative phosphorylation complex protein levels are largely unchanged at P9 in liver tissue homogenate. However, the protein expression of SDHB (complex II), MTCO1 (complex IV), and ATP5A (complex V) were reduced in tissue homogenate of P19 $Smn^{2B/-}$ livers (Figure 4A and B), highlighting a potential depletion of mitochondrion number. A reduced mitochondrial density was confirmed by lower activity of the citrate synthase (CS) enzyme at P19–21 (Figure 4C).[40] Cursory ultrastructural analysis of mitochondria revealed no obvious gross alterations (Figure 4D–G). We wondered whether the potential mitochondrial depletion observed may be related to autophagy or mitophagy. Upon analysis of low magnification electron microscopy images, we observed numerous vacuoles containing breakdown material likely representing autophagic process in the P19 control livers (Figure 4H and I). On the other hand, the P19 $Smn^{2B/-}$ livers showed propensity of fat globules that essentially overwhelmed most of the cells' histology, making it difficult to discern any vacuoles within these cells (Figure 4J). However, there was a remarkable contrast in cells that appeared less affected in $Smn^{2B/-}$ livers, containing multiple vacuoles with cellular debris (Figure 4K). In accordance with the lack of vacuoles observed in affected cells, we identified an accumulation of p62 (also known as sequestosome 1), a protein targeting waste product to the autophagosome (Figure 4L). This can be in keeping with inhibition of autophagy.[41] Nevertheless, it remains difficult to draw conclusions whether abnormalities in the autophagic/

mitophagic processes are at play. Because of the overwhelming space occupied by the fat droplet, we wondered whether this may lead to endoplasmic reticulum stress, a feature that has been associated with NAFLD.[42] In fact, a potential link between endoplasmic reticulum stress and impaired autophagic flux has previously been established in the context of NAFLD.[43] There was only a mild induction of activation transcription factor 4, but there was no clear induction of expression of other relevant endoplasmic reticulum stress proteins such binding-immunoglobulin protein, 94 kDa glucose-regulated protein, or C/EBP homologous protein (data not shown).

Next, we aimed to understand the functional capacity of the mitochondria in this setting. Surprisingly, high-resolution respirometry of isolated liver mitochondria from P19–21 $Smn^{2B/-}$ mice identified increased leak and adenosine diphosphate phosphorylation capacities when fueled by pyruvate, malate, and succinate (Figure 5A–E), or palmitoyl carnitine (data not shown). Interestingly, $Smn^{2B/-}$ mitochondrial function was similar to control mice at P9, a time point where hepatic fat accumulation is not readily observed.[24] Hepatic mitochondria from P9 and P19 $Smn^{2B/-}$ mice also exhibited an increase in reactive oxygen species (ROS) production (Figure 5F–J). It is possible that the increased capacity for respiration in isolated mitochondria from P19 $Smn^{2B/-}$ mice is a compensatory mechanism to restore metabolic homeostasis and/or in response to low mitochondrial density. In addition, the enhanced ROS production could be responsible in part for hepatocyte damage and death (Figure 1G–L). The increased capacity for fatty acid-supported respiration was consistent with the elevated levels of microsomal oxidation enzyme CYP4A (Figure 5K and L), known to be active upon β-oxidation overload.[6,44,45] Carnitine palmitoyl transferase I (CPT1), an enzyme responsible for shuttling long chain fatty acid into the mitochondria for β-oxidation, can be inhibited by malonyl-CoA, a product of de novo lipogenesis.[45] Such inhibition would lead to further fatty acid overspill in the microsomal oxidation pathway. We found CPT1 to have reduced activity in comparison with both WT and $Smn^{2B/+}$ mice at P19 (Figure 5M). Overall, our results show that mitochondrial function of isolated mitochondria pathologically increased in the $Smn^{2B/-}$ mice, when oxidative processes are supported directly by substrates for complexes I and II, leading to ROS production. Because CPT1 activity was decreased, it is possible that there is impaired formation of acyl carnitine

---

Figure 2. (See previous page). Liver function deficits are apparent in multiple pathways in symptomatic Smn²B/- mice. (A and B) Low levels of total protein and albumin in plasma from P19 $Smn^{2B/-}$ mice. (C and D) Major alterations in levels of transcripts for complement, hemostasis in livers from P19 $Smn^{2B/-}$ mice. (E) Iron metabolism genes are misregulated, with (F) associated concordant changes at the protein level of hepcidin and heme oxygenase but not transferrin. (G and H) Immunostaining of hepcidin (original magnification, ×63) was also reduced. (I) Iron levels are reduced in plasma but unchanged in liver (Prussian blue staining; original magnification, ×40) (J and K; arrowheads represent iron deposits). (L) Trend toward higher total bilirubin protein in plasma in $Smn^{2B/-}$ mice. (M–U) Iron loading showed more severe iron accumulation in the $Smn^{2B/-}$ livers. (V and W) Major alterations in expression of IGF1 pathway components, leading to progressive depletion of IGF-1 hormone in plasma from $Smn^{2B/-}$ mice. QPCR data were normalized with SDHA and PolJ (C, D, E, V). Scale bars represent 10 μm (G and H), 50 μm (J and K), and 200 μm (M–U). N value for each experiment is as follows: N = 8–10 for A, B, I, L, and W; 4–5 for C–E, F, J, K, M–U, and V; 3 for G and H; unpaired two-sided Student t test for all except for (W) two-way ANOVA with Sidak's multiple comparison test. *$P \leq .05$, **$P \leq .01$, ***$P \leq .001$, and ****$P \leq .0001$.
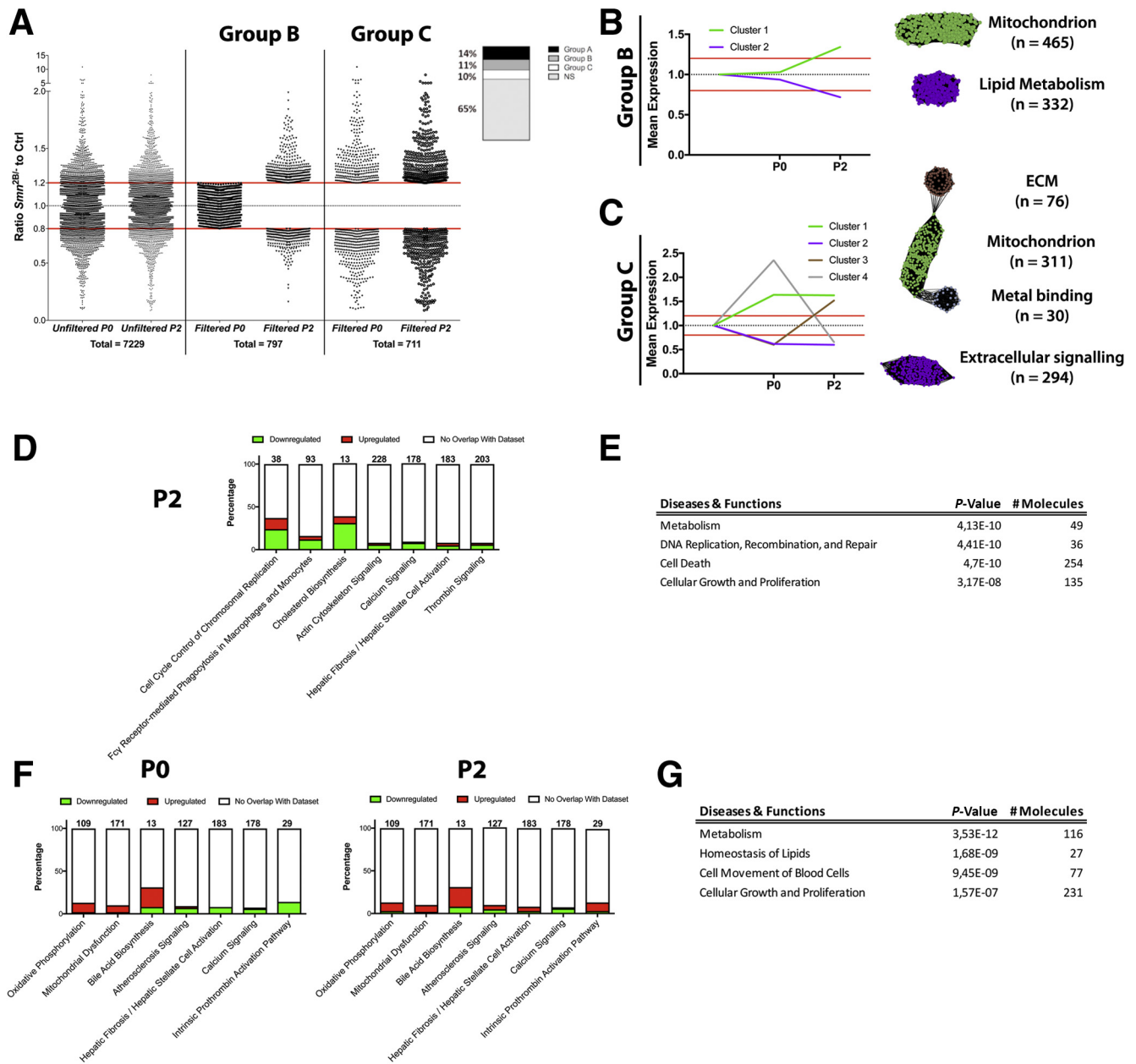
Figure 3. **Proteomic analysis of P0 and P2 Smn[2B/-] livers identifies mitochondrial and lipid metabolism as prominent perturbations.** (*A*) Scatter plots showing protein expression ratios of Smn[2B/-] to P0 WT (control) liver. A 20% threshold altered expression was applied. *Left column* of paired scatter plots shows Smn[2B/-] to WT ratios for 7229 proteins at birth (P0) and P2. Group B identified by filtering for proteins altered only at P2 in Smn[2B/-] livers (P0 = ns ($0.8 \leq x \leq 1.2$) and P2 = $P \leq .05$ (x < .8 or x > 1.2)). Group C filters for proteins altered at P0 and at P2 in Smn[2B/-] (P0 and P2 = $P \leq .05$ (x < .8 or x > 1.2). (*B* and *C*) Group B and Group C graphical representation of Smn[2B/-] to WT ratio proteins at P0 and P2, *left graph* before clustering, *right graph* after application of the MCL clustering algorithm (inflation value 2.2) analyzing coordinately expressed proteins. These are represented as mean ratio-change per cluster. In cluster visualization the proteins are spheres with correlation between them of $r \geq 0.9$ indicated by *black lines*. Each identified cluster has a functional annotation with n number stating how many proteins are present within the cluster. (*D*) IPA top canonical pathways highlighting the main disrupted cascades in Group B data set. *Stacked bar chart* displays the percentage of proteins that were up-regulated (*red*), down-regulated (*green*), and proteins that did not overlap with our data set (*white*) in each canonical pathway. *Numerical value at top of each bar* represents the total number of proteins in the canonical pathway. (*E*) Top diseases and functions linked to our Group B data set identified by IPA functional analysis. (*F*) IPA top canonical pathways highlighting the main disrupted cascades in Group C data set at P0 (left) and P2 (right). *Stacked bar chart* displays percentage of proteins that were up-regulated (*red*), down-regulated (*green*), and proteins that did not overlap with our data set (*white*) in each canonical pathway. *Numerical value at top of each bar* represents the total number of proteins in the canonical pathway. (*G*) Top diseases and functions linked to our Group C data set identified by IPA functional analysis.
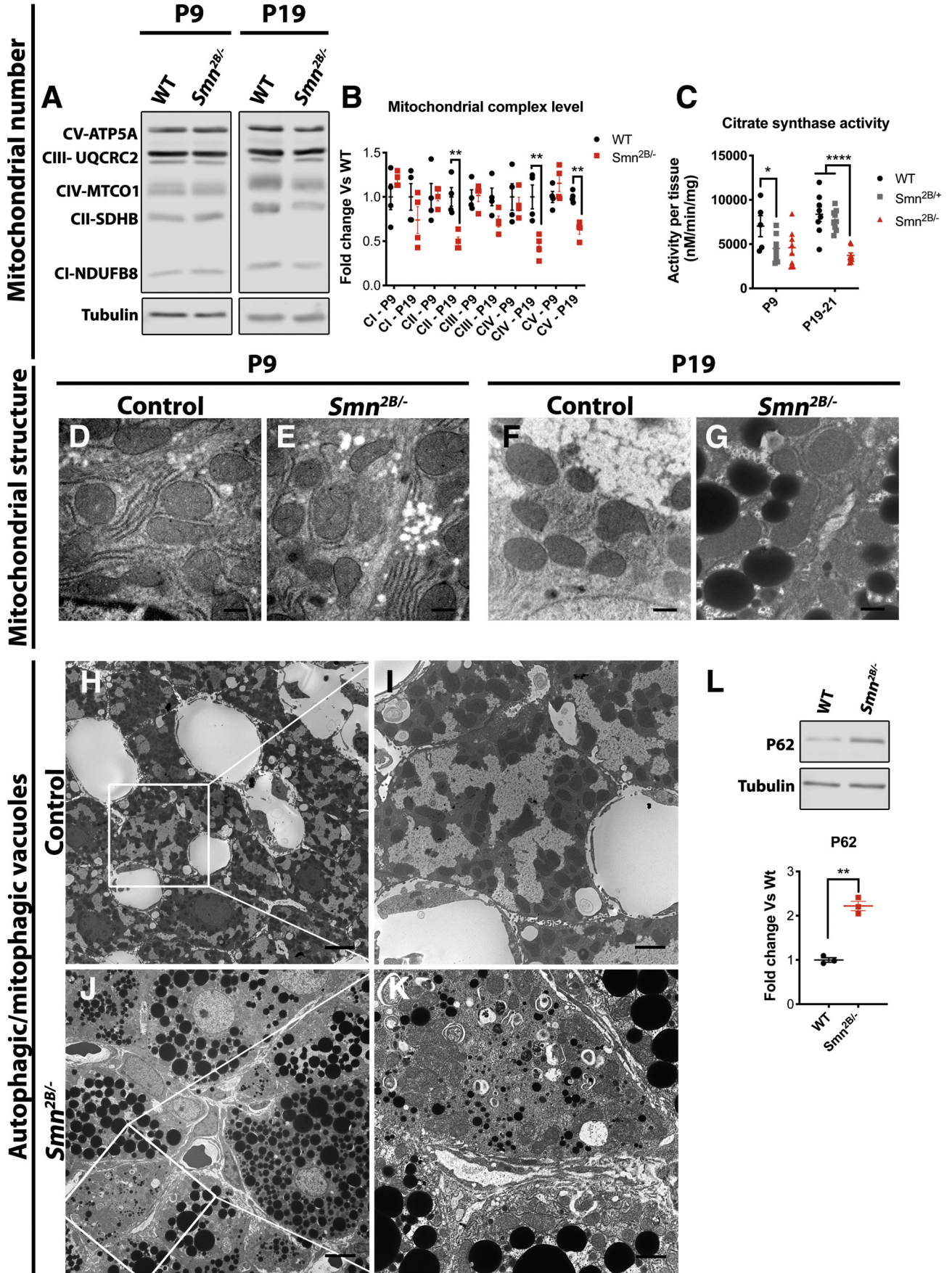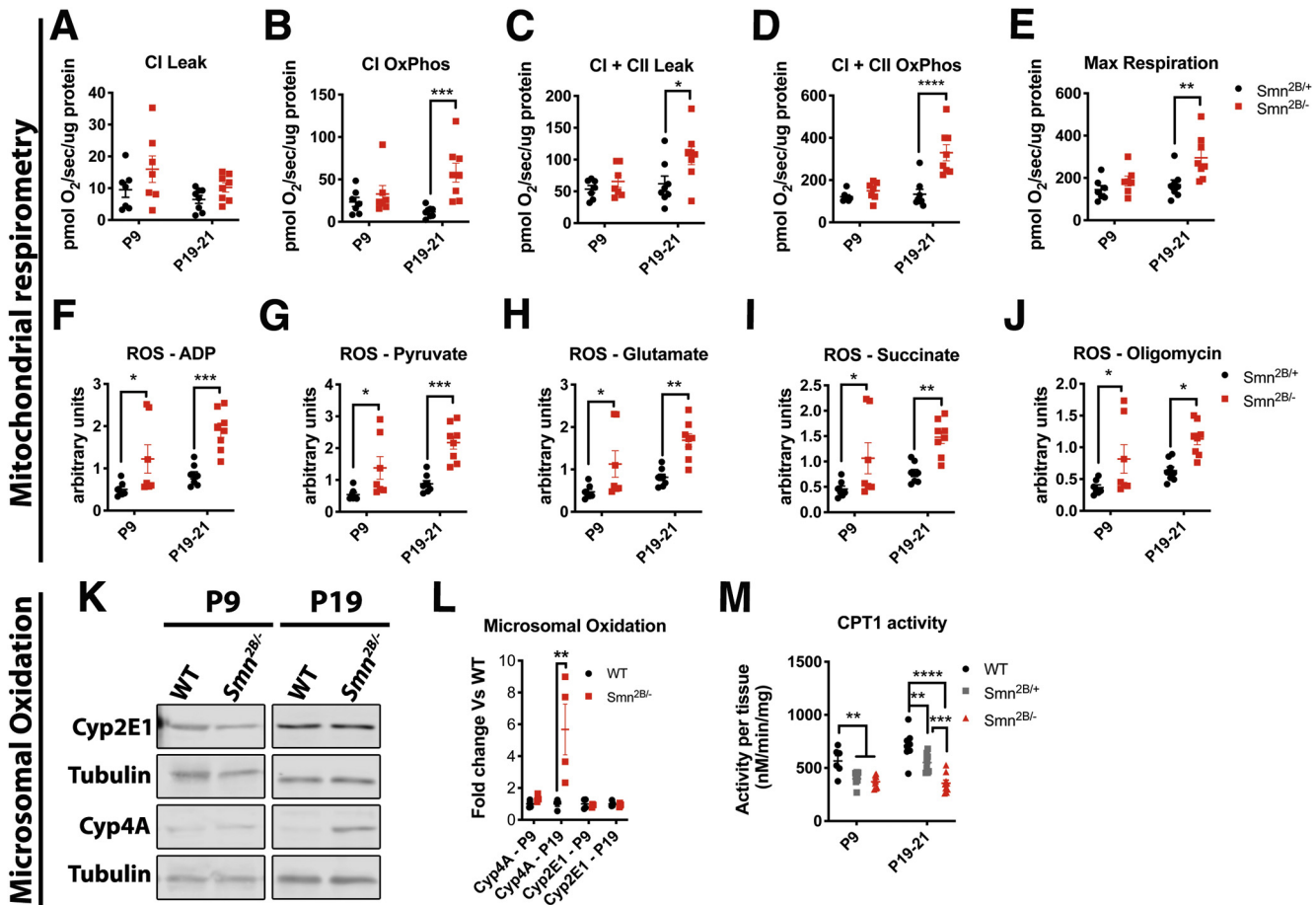
Figure 5. $Smn^{2B/-}$ liver mitochondria show increased β-oxidation and ROS production. (*A–E*) High-resolution respirometry of $Smn^{2B/-}$ hepatic mitochondria shows increased leak and higher respiratory capacity at P19 but not at P9 in comparison with $Smn^{2B/+}$ hepatic mitochondria. (*F–J*) $Smn^{2B/-}$ hepatic mitochondria had an increase in ROS production during most respiratory states in comparison with $Smn^{2B/+}$ mitochondria. (*K* and *L*) Increased expression of CYP4A is evident in P19 $Smn^{2B/-}$ livers. (*M*) Reduced CPT1 activity is present in livers of $Smn^{2B/-}$ mice compared with WT. N value for each experiment is as follows: N = 4 for *K* and *L*; 6–9 for *A–J*, *M*; two-way ANOVA with Sidak's multiple comparison for all except *M*, two-way ANOVA with Tukey's multiple comparison tests. *$P \leq .05$, **$P \leq .01$, ***$P \leq .001$, and ****$P \leq .0001$.

species or inhibition of CPT1 activity, activation of proton leak, and reduced uptake of long chain fatty acids for mitochondrial oxidation in vivo, further exacerbating hepatic steatosis.

Hormonal Contribution to NAFLD in Smn²B/- Mice

Insulin insensitivity plays a major role in the development of NAFLD. $Smn^{2B/-}$ mice show abnormal glucose handling in intraperitoneal glucose tolerance test.[46] Surprisingly, the $Smn^{2B/-}$ mice show sustained hypoglycemia with age in normoinsulinemic state and a trend toward diminished C-peptide production at P19 (Figure 6A–C). Because of their small size and age, hyperinsulinemic clamp is not feasible to further assess insulin sensitivity. However, $Smn^{2B/-}$ mice show hepatic insulin resistance as demonstrated by lowered ability to phosphorylate protein kinase B (Akt) on administration of insulin (Figure 6D and E). This may be related to the low IGF1 production by the liver.[47]

Figure 4. (*See previous page*). **Reduced mitochondrial density in P19 $Smn^{2B/-}$ livers.** (*A* and *B*) Western blot analysis of subunits of the mitochondrial complexes shows no significant change before hepatic fat accumulation at P9 but shows significant down-regulation of CII, CIV, and CV subunit proteins in P19 $Smn^{2B/-}$ liver homogenates. (*C*) Lower CS activity in livers of P19–21 $Smn^{2B/-}$ mice suggests decreased mitochondrial density per mg of tissue. (*D–G*) Mitochondrial structure appears relatively spared at both P9 and P19 in $Smn^{2B/-}$ livers. (*H–K*) Potential lower propensity of autophagic/mitophagic vacuoles in P19 $Smn^{2B/-}$ livers because of intense fatty infiltration, where less affected cells appear to retain some vacuoles. (*L*) p62 elevation in P19 $Smn^{2B/-}$ livers potentially contributes to autophagic blockade. Scale bar represents (*D–G*) 500 nm, (*H* and *J*) 6 μm, and (*I* and *K*) 2 μm. N value for each experiment is as follows: N = 3–4 for *A* and *B*, *D–G*, and *H–L*; 5–9 for *C*; two-way ANOVA with Sidak's multiple comparison for *A* and *B*, two-way ANOVA with Tukey's multiple comparison tests for *C*, two-sided Student *t* test for *L*. *$P \leq .05$, **$P \leq .01$, ***$P \leq .001$, and ****$P \leq .0001$.

Alternatively, we also noted a progressive elevation of plasma glucagon levels, which was first evident at P11 in $Smn^{2B/-}$ mice (Figure 6F). This increase in glucagon likely results from the increase in alpha-cell number in $Smn^{2B/-}$ pancreas[46] and/or low glucose. Glucagon signaling mediates some of its effects through the phosphorylation of Creb, which leads to expression of the gluconeogenic program.[48] We observed increased phospho-Creb levels in livers of P19 $Smn^{2B/-}$ mice (Figure 6G and H). Interestingly, there is a robust increase in the levels of glucagon-like peptide-1 (Figure 6I), another byproduct of proglucagon, produced in the gastrointestinal tract. We further investigated adipocytic hormones (ie, leptin, adiponectin), which are known to play a role in NAFLD/NASH progression and fibrosis.[6] We did not observe any changes in leptin or adiponectin in $Smn^{2B/-}$ mice (Figure 6J and K), which is in keeping with minimal evidence of fibrosis on histology in these mice. Other hormones from the gastrointestinal tract (ghrelin, GIP), pancreas (PP, amylin), and adipocyte (resistin) did not show a consistent pattern of misregulation, apart from PYY (GI) (Figure 7).

Enhanced glucagon levels/signaling lead to glycogenolysis and gluconeogenesis in the liver and lipolysis in the white adipose tissue to increase energetic substrate availability in the bloodstream.[49] Pathologic glucagon signaling could lead to energy substrate overload in the blood and subsequent stimulation of the liver to restore homeostasis via uptake of these substrates, including lipids. Although limited change was identified in the timeframe of acute fat accumulation in the liver on pathology (between P11-13[24]) (Figure 8C–F), we observed eventual hepatic glycogen depletion at P19 (Figure 8A and B), a trend toward adipocyte size reduction (Figure 8G–M), and increased non-esterified fatty acid (NEFA) (Figure 8N), a direct product of lipolysis, in the blood. These findings are consistent with enhanced glucagon signaling. More particularly, NEFA level was readily observable at P11 and worsened over time in comparison with control (Figure 8N). Triglyceride levels followed a similar progression, albeit in a delayed fashion (Figure 8O). Altogether, these findings point to a fatty substrate overload in the blood as a consequence of glucagon pathway activation in the context of insulin resistance.

Discussion

We systematically characterized typical features of NAFLD development in the $Smn^{2B/-}$ mice. The mice develop microvesicular steatohepatitis within 2 weeks of life, with increased serum markers of liver damage, hepatocyte cell death, molecular signs of fibrogenesis, and hepatic stellate cell activation without established fibrosis. The $Smn^{2B/-}$ mice also display significant dyslipidemia (elevated total cholesterol, VLDL and LDL and reduced HDL),[24] peripheral lipolysis, functional hepatic deficits, alterations in mitochondrial function, evidence of involvement of alternative oxidative pathways, and ROS production in the liver. All of these features have been observed in NAFLD.[6] Nevertheless, the $Smn^{2B/-}$ mouse as a model for NAFLD also has some limitations. (1) Although they show many molecular changes in

genes involved in the fibrogenic process and hepatic stellate cell activation, they do not develop fibrosis, a component that is seen in NASH patients.[6] It is possible that they could go on to develop fibrosis after prolonged hepatic damage; however, their lifespan of 25 days[18] is likely too short to lead to a fibrotic phenotype. (2) $Smn^{2B/-}$ mice also lose weight because of their associated neurological condition. Interestingly, although NAFLD presentation often occurs in tandem with obesity, it also presents in individuals without weight gain.[1] Sedentary lifestyle (or immobility) is a risk factor for NAFLD,[50] and exercise can sometimes prevent the NAFLD phenotype in preclinical models fed high-fat diet.[51] The lack of muscle use, whether from a pathogenic event (due to SMA) or by choice, may be necessary for adequate development of the phenotype. This is highlighted by the development of a mouse model with a sedentary lifestyle component such as the American Lifestyle-Induced Obesity Syndrome model.[52] (3) $Smn^{2B/-}$ mice display low blood sugar and normal insulin levels but show evidence of insulin resistance. Although most NAFLD patients have most components of metabolic syndrome, which includes features of obesity, dyslipidemia, insulin resistance, hyperglycemia, and hyperinsulinemia,[6] we report that the $Smn^{2B/-}$ mice also show features of an incomplete metabolic syndrome phenotype (insulin resistance and dyslipidemia).

In comparison, some popular NAFLD models also show limitations. For example, the MCD diet model does not exhibit any of the metabolic features.[6,10,11,14] The ob/ob and db/db mutant mice, which display altered leptin signaling, have metabolic features but no inflammation or fibrosis.[6,10,11] The high-fat diet appears to result in all features of the NAFLD spectrum; however, fibrosis is minimal and can take up to 36–50 weeks to develop.[53] As such, the $Smn^{2B/-}$ mice could provide an efficient mouse model of NAFLD because of its fast-onset steatosis phenotype, paired with the fact that no special and expensive diet is required, making it a cost-effective option. In fact, introduction of high-fat diet did not drastically worsen the overall metabolic phenotype of the $Smn^{2B/-}$ mice,[54] but studies were limited to biochemical measures. In addition, our study made use of both male and female mice, unlike other mouse models where males are predominantly used.[55] Needless to say, the $Smn^{2B/-}$ mice would allow for a different outlook on molecular players and organ system involvement in comparison with current available models of NAFLD. Indeed, the $Smn^{2B/-}$ mice could act as one of the few mouse models for pediatric NAFLD and/or microvesicular steatosis.[55,56] To our knowledge, all current NAFLD models mostly display macrovesicular steatosis, apart from the $Acox^{-/-}$ mice, which develop predominantly microvesicular steatosis.[57]

Despite not progressing to the most severe phenotype of cirrhosis, the functional analysis revealed significant changes at multiple levels. There was a reduction in total protein production, albumin production, complement expression, coagulation components, and IGF1 pathway members. These changes are likely to represent a reduced synthetic potential of the damaged hepatocytes. In patients with failing liver, this low synthetic function can lead to a whole array of physical symptoms.[58] Interestingly, this is
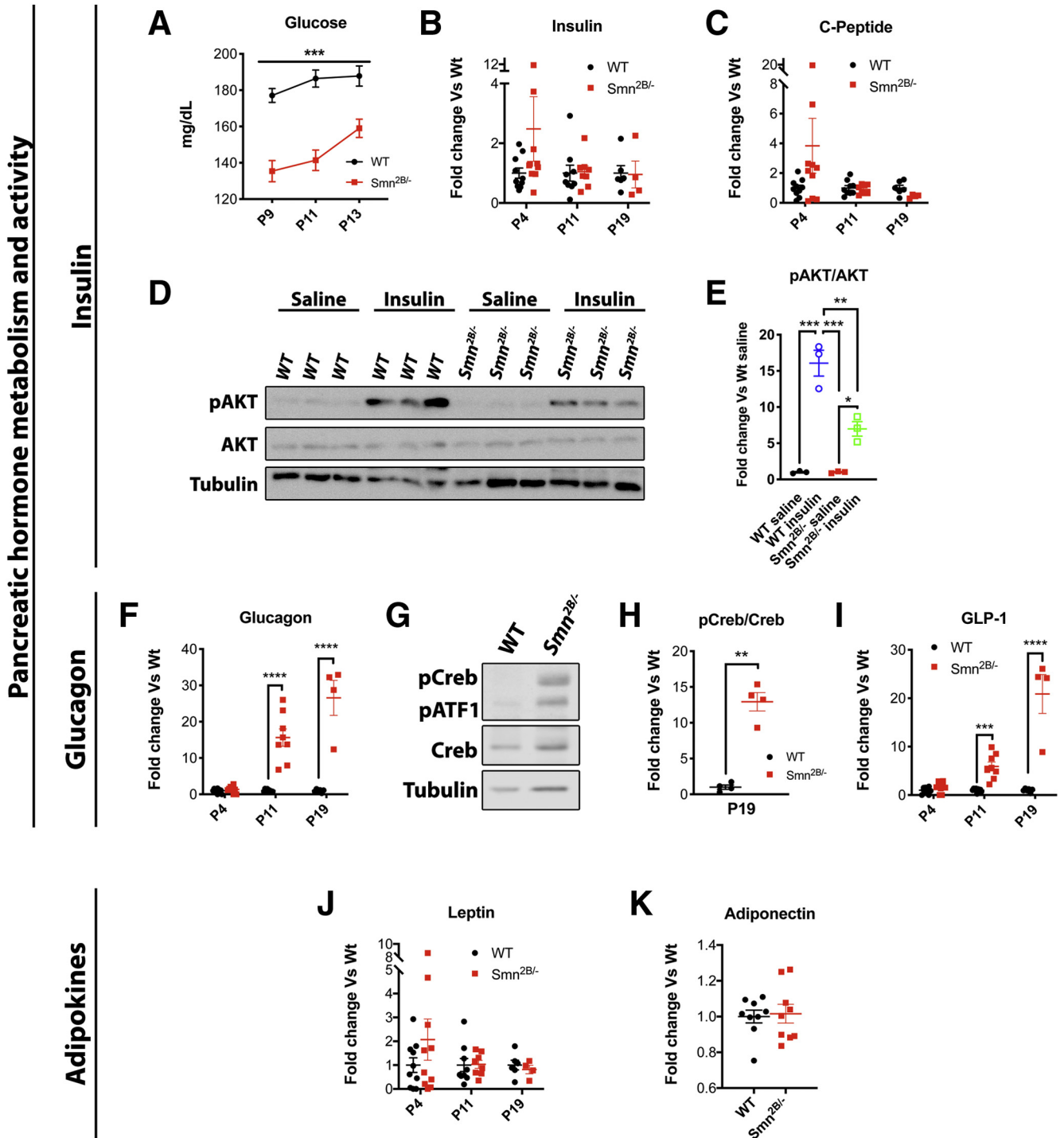
Figure 6. Impaired insulin and glucagon pathways in Smn[2B/-] mice. (*A*) Plasma glucose was lower throughout P9 to P13 in Smn[2B/-] mice in comparison with WT mice. (*B*) Insulin levels were relatively maintained throughout the Smn[2B/-] mice lifespan. (*C*) Trend toward diminished C-peptide production is only seen at P19 in Smn[2B/-] mice. (*D* and *E*) Insulin sensitivity is about half the capacity of control animals as shown by reduced Akt phosphorylation (Ser473) in livers of P19 Smn[2B/-] mice. (*F*) Progressive elevation of plasma glucagon occurs in Smn[2B/-] mice with ~15-fold increase by P11. (*G* and *H*) Western blot analysis shows about a 12-fold increase in phospho-Creb, a downstream molecular event of glucagon activation, in P19 Smn[2B/-] livers in comparison with WT. (*I*) Plasma GLP-1, a product of the cleavage of proglucagon, is altered in a similar fashion. (*J* and *K*) Adipokines leptin and adiponectin levels remained relatively unchanged. N value for each experiment is as follows: N = 8–10 in *A, K*; 8–10 for P4, P11; and 4–6 at P19 in *B, C, F, I, J*; 3 in *D* and *E*; and 4 in *G* and *H*; two-way ANOVA with Sidak's multiple comparisons test for *A–C, F, I, J*; one-way ANOVA with Tukey's multiple comparison tests for *D* and *E*; unpaired two-sided Student *t* test for *G, H, K*. *$P \leq$ .05, **$P \leq$ .01, ***$P \leq$ .001, and ****$P \leq$ .0001.
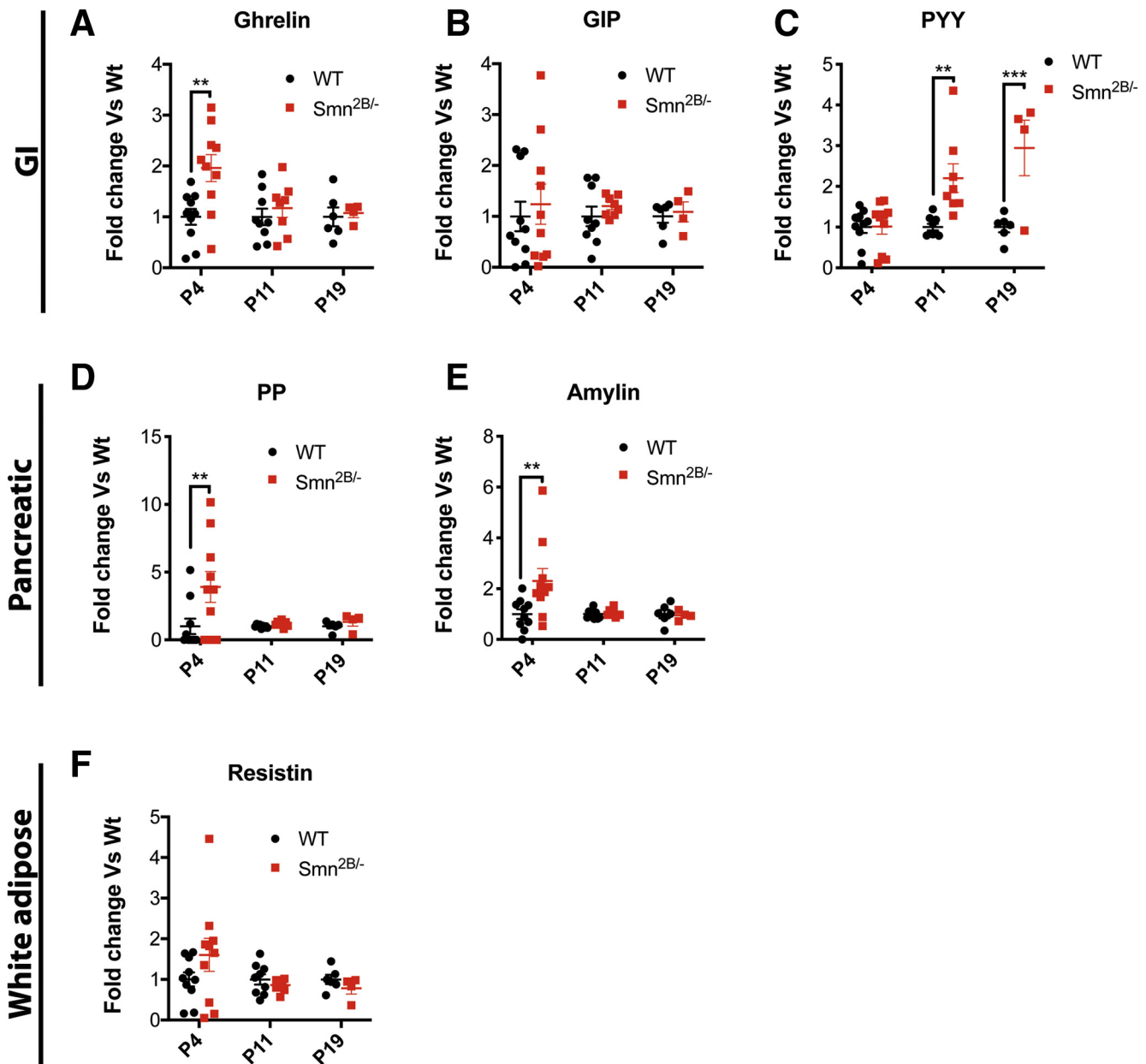
Figure 7. Other metabolic hormone levels are largely unchanged in the plasma of Smn$^{2B/-}$ mice. (*A–C*) PYY is the only significantly changed hormone originating from the gastrointestinal system, whereas ghrelin and GIP were largely unchanged. (*D* and *E*) Minor differences are present in pancreatic hormones. (*H–J*) No changes in resistin were observed. N value for each experiment is as follows: N = 8–10 for P4, P11 and 4–6 at P19 in *A–F*; two-way ANOVA with Sidak's multiple comparisons test. *$P \leq .05$, **$P \leq .01$. GI, gastrointestinal.

thought to be mediated by important hepatic transcription factors such as HFN4a in preclinical models[30] and human patients.[31] Many of the abnormal hepatic synthetic functions, but also the overall survival and phenotype, can be partially reversed by forced expression of HFN4a back into the organism.[30] We found HNF4a to be reduced in Smn$^{2B/-}$ mice in a similar fashion to those with severe liver disease. On the other hand, the etiology of IGF1 pathway and iron metabolism deficits is much less clear. IGF1 has been linked to liver disease in multiple studies, where its levels are generally observed to be low.[39,59] Interestingly, IGF1

depletion may lead to insulin sensitivity.[47,60] It is unclear whether IGF1 reduction is an initiator or a consequence of NAFLD. We suspect that the reduction of IGF1 is consequent of the reduced synthetic capacity and impaired stability of the remaining protein. The inability to form a stable complex of binding IGF1, IGF-binding protein 3, and IGFals likely significantly impacts its degradation kinetics in light of the major difference in half-life bound to this complex vs unbound (~10 minutes vs 15 hours, respectively).[60,61] Iron status in NAFLD is also a notion that surfaced on many occasions. Iron is thought, with some conflicting evidence in
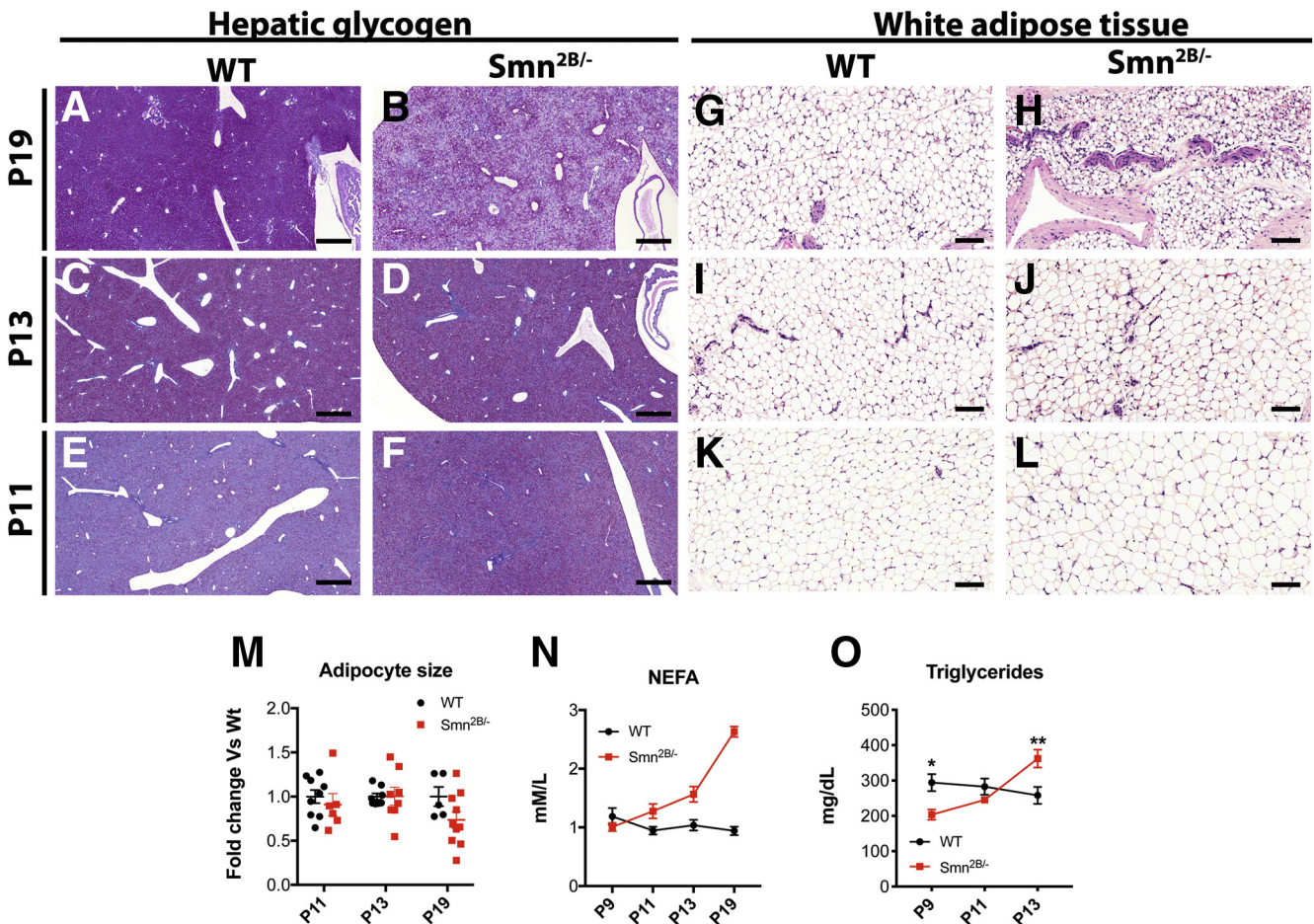
Hepatic glycogen

WT   Smn[2B/-]

White adipose tissue

WT   Smn[2B/-]

Figure 8. Hyperglucagonemia leads to increased substrate release in the plasma of Smn[2B/-] mice. (A–F) Periodic acid-Schiff stained liver sections (5×) at P19, P13, and P11 reveal glycogen depletion in P19 Smn[2B/-] mice (A and B) but not at P13 (C and D) and P11 (E and F). (G–L) H&E sections (20×) of subcutaneous adipose tissue show a trend toward reduction in adipocyte size at P19 Smn[2B/-] mice (G, H, M) but not at P13 (I, J, M) and P11 (K–M). (N) Plasma NEFA progressively increases from P9 to P19, concordant with increased lipolysis of white adipose tissue. (O) Plasma triglyceride quantification showed similar trend as NEFA, albeit in a delayed fashion. Scale bar represents 500 μm in (A–F) and 100 μm in (G–L). N value for each experiment is as follows: N = 8–10 in N and O; 5 for A–F; 5–10 for G–M; two-way ANOVA with Sidak's multiple comparisons test for M and O; note that no statistical analysis was performed on N because of results obtained through different techniques for P19. *$P \leq .05$, **$P \leq .01$, ***$P \leq .001$, and ****$P \leq .0001$.

humans, to potentially play a role in the development of NAFLD.[32] However, the wealth of research tends to implicate iron in NAFLD when a surplus of iron or overload is present, with attempts to diminish iron load to improve the metabolic phenotype.[32] Our model rather presents with normal to low iron stores.

Microvesicular steatosis is present in all Smn[2B/-] mice. It is only present in a minority of adult NAFLD patients (10%) and associated with more severe disease.[5] In the pediatric population, microvesicular steatosis is generally clinically associated with inherited metabolic disorders and fatty acid oxidation defects.[62] We found no evidence of a β-oxidation deficit in our model using high-resolution respirometry in isolated liver mitochondria. On the contrary, it appears that the isolated mitochondria have enhanced capacity, perhaps reflective of a compensatory reaction to the reduced mitochondrial density and the increase in triglyceride storage. Nevertheless, our proteomic screen identified alterations in

2 important clusters, namely mitochondria and lipid metabolism, close to birth and well before any overt neurological or hepatic pathology develops. Interestingly, mitochondrial pathway components are often represented in "omic" data of SMN depleted tissue,[63–68] and mitochondrial defects have previously been reported in cell culture and SMN depleted models.[68–71] In addition, it is also part of NAFLD/NASH pathogenesis.[6] As such, additional investigation will be required to refine mitochondrial defects in this model and how it can relate to NAFLD/NASH.

From our analysis, we conclude that NAFLD development in Smn[2B/-] mice is multifactorial. The proposed mechanism underpinning the defects is illustrated in Figure 9. We propose that the initial event leading to fatty acid dysregulation in the liver likely stems from abnormal glucose homeostasis. Hyperglucagonemia is induced early in Smn[2B/-] mice in response to low blood glucose in the bloodstream or from the pathologic overpopulation of alpha
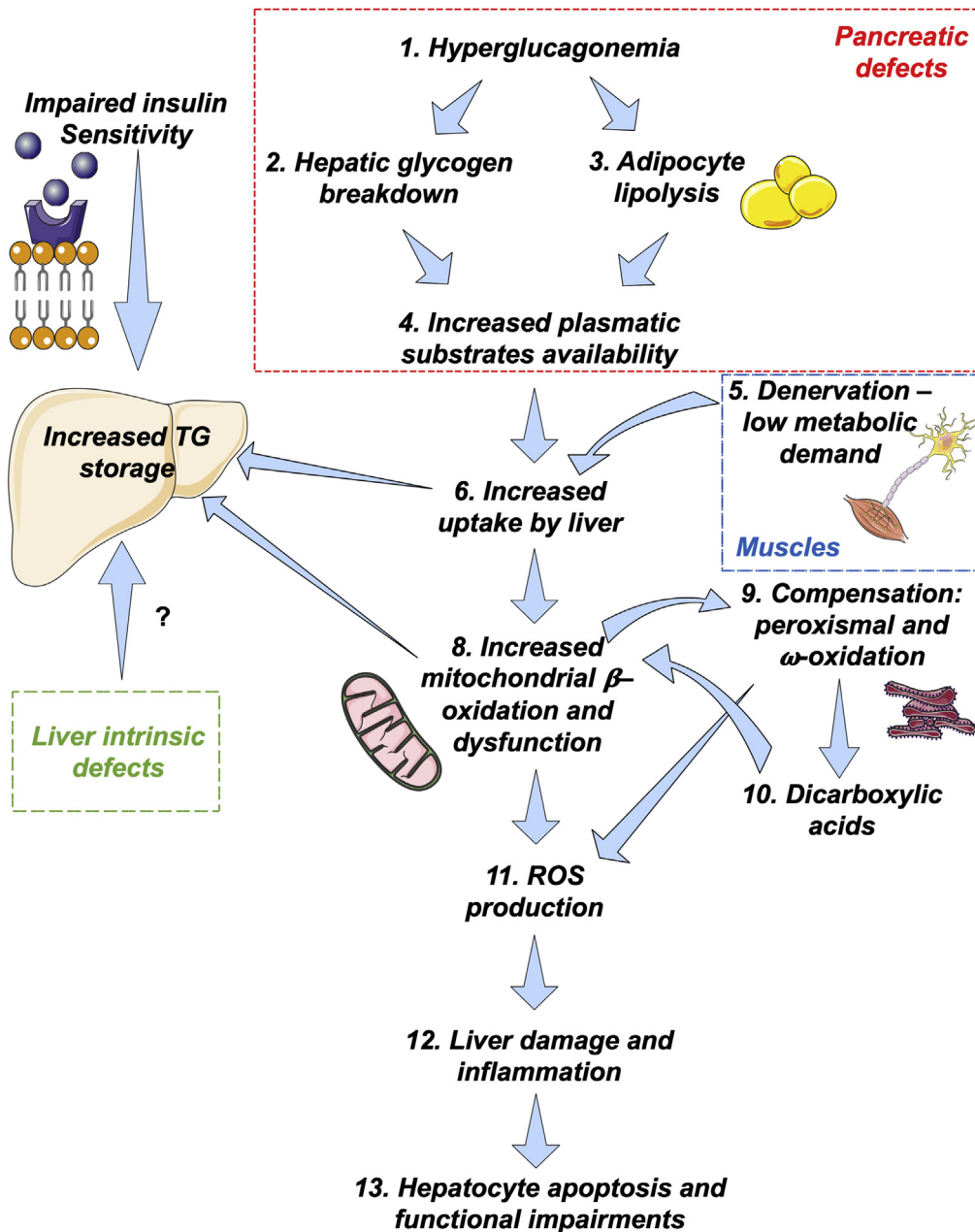
Figure 9. Schematic summarizing the findings of the present study. Undefined glucose/pancreatic abnormalities lead to hyperglucagonemia, leading to hepatic glycogen breakdown and adipocyte lipolysis in the context of hepatic insulin resistance. This results in increased plasma energy substrate availability before or concomitantly to muscle denervation, the major user of energy in the blood. This leads to overload of fatty substrates in the blood, which the liver takes up to restore homeostasis, leading to steatosis. To compensate and dispose of the unnecessary lipids, mitochondrial oxidation is increased to burn excess lipids, which eventually becomes overloaded and requires alternative peroxisomal and microsomal oxidation pathway. Such compensation leads to increased ROS production, liver damage, hepatocyte apoptosis, and eventually functional impairment. The schematic art pieces used in this figure were provided by Servier Medical art, https://smart.servier.com. Servier Medical Art by Servier is licensed under a Creative Commons Attribution 3.0 Unported License.

cells in the pancreas.[46] Surprisingly, glucose levels in the $Smn^{2B/-}$ mice are reduced as early as P9. The glucose level remains low but is sustained, likely because of gluconeogenesis. Eventually, gluconeogenesis fails because of depleted glycogen storage in P19 $Smn^{2B/-}$ mice, leading to a sudden drop in glucose level in the blood.[24] Simultaneously, lipolysis of white adipose tissue, a byproduct of glucagon signaling, is induced to ensure availability of energy substrate, represented by a progressive increase in NEFA from P9 to P19 in $Smn^{2B/-}$ mice. This leads to increased fatty substrates in the bloodstream, which precede or coincide with muscle denervation. Skeletal muscle, a major consumer of energy substrates when innervated and fully functional, will have a diminished requirement for energy as denervation renders it nonfunctional in SMA. As such, this leads to

overload of fatty energy substrates in the circulation in a state of insulin resistance. Eventually, the susceptible liver will take up the lipid substrates for storage in an attempt to restore homeostasis, which in turn leads to liver steatosis. Pathologic fat storage could spill over to the muscle compartment once the liver has reached saturation, which is consistent with our previous description of lipid droplets on ultrastructural analysis of skeletal muscle of $Smn^{2B/-}$ mice.[72] Finally, enhanced ROS production from mitochondrial oxidation leads to hepatic damage and functional deficits. From a molecular perspective, the link between SMN and NAFLD is not clear. SMN has an essential role in pre-mRNA splicing, among other housekeeping functions in the cells.[23] As such, SMN depletion has far-reaching effects on the transcriptome and cellular activity. Transcriptomic analysis

of various SMN depleted tissue identified the liver to be the most abnormal.[20] The direct targets of SMN in the liver are unknown at this time. In addition, SMNs likely have to be cell-specific consequences, and intrinsic defects of cells from other metabolic organs may be at play. A comprehensive analysis of transcriptomic data of relevant metabolic tissues involved in NAFLD will be key in identifying player contributory to its phenotype.

Altogether, $Smn^{2B/-}$ mice will provide an appropriate NAFLD model. It can be leveraged for high throughput identification of molecular pathways involved in NAFLD because of the fast onset of the phenotype (less than 2 weeks) and the lack of a required diet, making it a cost-effective option in the study of NAFLD pathogenesis.

Materials and Methods

Study Design

We have recently identified the increased prevalence of dyslipidemia and fatty liver[24] in SMA patients and SMA mouse models. This sparked a project with the following 2 prespecified objectives: (1) identify consequences of the fatty acid defect and (2) identify the etiology of these defects and how it relates to NAFLD pathogenesis. As it pertains to this article, the etiologies of the defects were suspected on prior experience with this SMA mouse model and NAFLD literature. It included denervation,[24] liver-intrinsic defects, mitochondrion, and external factors (other organs). Serum analysis and lipid quantification were outsourced; thus, analyses were performed in a blinded fashion. Numbers are described in each figure legend. Statistical approach is as described below and in figure captions. Collaboration between laboratories of Kothary and Parson and colleagues occurred mid-project because of overlapping results that were converging. Hence, the resulting article offers data that have been concordant in 2 independent laboratories (albeit using different experimental paradigms).

Mouse Models

The $Smn^{2B/-}$ (WT C57BL/6J background)[18] mouse lines were housed at the University of Ottawa Animal Facility and cared for according to the Canadian Council on Animal Care. Experimentation and breeding were performed under protocol OHRI-1948 and OHRI-1927. $Smn^{+/-}$ mice were crossed to $Smn^{2B/2B}$ mice to obtain $Smn^{2B/+}$ and $Smn^{2B/-}$ animals. C57BL/6J WT mice were bred separately. All experiments using mice in the United Kingdom were performed in accordance with the licensing procedures authorized by the UK Home Office (Animal Scientific Procedures Act 1986). All tissues in the Kothary laboratory were collected while mice were fed ad libitum. Tissues undergoing biochemical analysis in the Kothary laboratory were collected between 9 and 11 AM to limit the effect of the circadian rhythm.

Production and Administration of scAAV9-CB-SMN or ssAAV9-hIGF1

The scAAV9-CB-SMN vectors were produced at the Bertarelli Platform for Gene Therapy in EPFL (Gstaad, Switzerland), using a construct similar to the one described elsewhere.[73] The self-complementary scAAV9-CB-SMN and ssAAV9-hIGF1 vectors were produced by calcium phosphate transfection of HEK293-AAV cells (Agilent, Santa Clara, CA) with pAAV-CB-SMN[73] or pAAV-hIGF1 and pDF9 plasmids. Briefly, the vector was purified from the cell lysate using an iodixanol density gradient, followed by anion exchange chromatography (HiTrap Q-FF column; GE Healthcare, Chicago, IL). The scAAV9-CB-SMN or ssAAV9-hIGF1 vector was finally resuspended and concentrated in Dulbecco phosphate-buffered saline (PBS) on a centrifugal filter unit (Amicon Ultra-15; Millipore, Burlington, MA). The titer of the vector suspensions was determined by quantitative polymerase chain reaction (qPCR) using an amplicon located in the inverted terminal repeats as described elsewhere.[74] The obtained titers of the scAAV9-CB-SMN vectors were 9.6^{13} VG/mL and 3.0^{13} VG/mL. The obtained titers of the AAV9-hIGF1 vectors were 1.5^{14} VG/mL. $Smn^{2B/-}$ and $Smn^{2B/+}$ mice were injected with 5×10^{10} VG of the AAV9-CB-SMN or AAV9-hIGF1 viral vector at P1 through the facial vein, and the mice were then allowed to age until P19.

Insulin Sensitivity

Protocol was performed as described elsewhere[42] with slight modifications. Briefly, P19 WT and $Smn^{2B/-}$ mice were fasted for 4 hours. They subsequently received intraperitoneal injection of 2 U/kg insulin (Novolin ge Toronto 100 IU/mL, human) and were sacrificed 20 minutes later for tissue collection. Livers were then collected for protein analysis and probed for pAKT, total AKT, and tubulin.

Iron Loading

The protocol was carried out as previously published.[75] Briefly, P12 $Smn^{2B/+}$ and $Smn^{2B/-}$ mice received intraperitoneal injection of 250 μg iron dextran (Sigma-Aldrich, St Louis, MO; cat# D8517) per g body weight. Seven days after injections, the mice were sacrificed for collection of the liver for histologic analysis with Prussian blue.

Gross Morphology, Tissue Processing, and Staining of Animal Tissues

Livers and white adipose tissue were fixed in formalin (1:10 dilution buffered, from Protocol; cat #245-684) for 24–48 hours or 72 hours (white adipose tissue) at 4°C and then transferred in 70% ethanol at 4°C until processing. All samples used for histologic assessment were processed at the University of Ottawa (Department of Pathology and Laboratory Medicine) and embedded in wax using a LOGOS microwave hybrid tissue processor. Paraffin block tissues were cut with a microtome at 3- to 4-μm thickness. H&E staining was performed using a Leica autostainer XL (Leica Biosystems, Buffalo, IL). Periodic acid-Schiff, Prussian blue, oil red O, and Sirius red staining were performed using standard methods. Staining for platelets, neutrophils, and hepcidin were performed in the Kothary laboratory. Briefly, the paraffinized sections were deparaffinized in 3 changes of xylene substitute Histo-Clear (Fisher Scientific, Waltham, MA; 50-899-90147) for 10 minutes each, followed by 2

changes in a 50/50 mixture of absolute ethanol and Histo-Clear for 3 minutes each. Sections were gradually rehydrated in 100%-95%-70%-50%-0% ethanol. A heat-induced antigen retrieval step was performed when needed using Tris/EDTA buffer, pH 9.0 or sodium citrate buffer, pH 6.0. Sections were permeabilized with 0.1% Triton X-100 (Sigma-Aldrich) for 5 minutes and then blocked 1 hour in blocking buffer (10% goat serum, 1% bovine serum albumin, and 0.1% Triton X-100 in PBS). Slides were incubated with primary antibodies alone or in combination NIMP-R14 (Abcam ab2557, Cambridge, UK; 1:100), Hepcidin-25 (Abcam ab75883, 1:250), CD-41 (Abcam ab225896, 1:100-250), and alpha smooth muscle actin (Abcam, ab7817, 1:250) diluted in a first dilution buffer (1% bovine serum albumin, 0.1% Triton x-100 in PBS) for 90 minutes at room temperature. Sections were subsequently washed 3 times in PBS for 15 minutes and then incubated with the secondary antibodies Alexa Fluor-488, Alexa Fluor-555 (Invitrogen, Carlsbad, CA; 1:250) diluted in a second dilution buffer (10% goat serum, 0.01% Triton X-100 in PBS) for 1 hour at room temperature. Sections were washed in PBS for 5 minutes and counterstained with 4′,6-diamidino-2-phenylindole, dihydrochloride (DAPI; Molecular Probes, Eugene, OR; D1306, 1:5000) for 5 minutes. Slides were washed 2 times in PBS for 10 minutes and mounted with fluorescent mounting medium (DAKO mounting medium; Agilent). Pictures were acquired using microscope Zeiss Axio Imager M1 (Oberkochen, Germany) mounted with a digital camera. Tissue undergoing immunofluorescence for caspase 3 and collagen IV were processed in Dr Parson's laboratory. The tissues for immunofluorescence staining were sectioned (5 μm) on a cryostat (Leica, CM3050 S) or a microtome (Leica, RM2125 RTS). Liver sections were stained for caspase 3 (Abcam Ab13847 1:100) and collagen IV (Millipore AB756P 1:100). Antigen retrieval was performed to visualize Casp3. Briefly, air-dried sections were quickly washed in PBS and then submerged into prewarmed Antigen Retrieval Buffer and placed into water bath set at 90°C for 40 minutes (caspase 3). The sections were removed from the bath but left submerged in the buffer, allowing them to cool down but not dry out. After approximately 30 minutes, the slides were quickly washed in PBS and subjected to the traditional immunohistochemistry staining protocol. Acquisition of signal was either obtained by slide scanning with a MIRAX MIDI digital slide scanner (Zeiss) and images acquired using 3DHISTECH Panoramic Viewer 1.15.4/CaseViewer 2.1/ZenBlue 3.2 or directly captured using a Nikon (Tokyo, Japan) eclipse e400 microscope (×10, ×20, or ×40 objective) and its images captured using QICAM Fast 1394 camera and Improvision Velocity 4 image capture software.

Gene Expression Studies and PCR Array

RNA from liver was extracted using Qiagen (Hilden, Germany) RNeasy Mini kit and reverse transcribed using RT² first strand kit according to manufacturer's protocol. A complete list of primers is available in Supplementary Table 1. A standard curve was performed for each primer set to ensure their efficiencies. Each qPCR reaction contained equal amount of cDNA, Evagreen SyBR (Bio-Rad, Hercules, CA), RNase/DNase-free water, and appropriate primers (100–200 nmol/L or according to PrimePCR protocol) in a final volume of 25 μL or 20 μL (for primePCR primers). To confirm amplicon specificity, a melting curve analysis was performed. Two negative controls were included in every qPCR plate and consisted of water in lieu of cDNA. The qPCR results were quantified using $2^{-\Delta\Delta Ct}$ method. Results were normalized with 2 genes (mentioned in each figure legend containing qPCR data) identified as appropriate stable internal reference given M value below 0.5 and coefficient of variance below 0.25. PCR arrays for mouse fibrosis were purchased at Qiagen (PAMM-120Z) and were performed according to the manufacturer's protocol. Analysis was performed using their analysis platform (https://geneglobe.qiagen.com/us/analyze/). Genes for normalization were manually selected to identify minimal difference in geometric means, and Gapdh, Actb, and Hsp90ab1 were selected (geometric mean 23.54 vs 23.55 in control vs $Smn^{2B/-}$). P values were directly obtained from the analysis platform.

Immunoblotting

Total protein lysate was collected by homogenization of flash frozen liver in RIPA lysis buffer (Cell Signaling Technology, Danvers, MA). Protein concentrations were determined using the Bradford assay (Bio-Rad) or BCA assay. Protein extracts were subjected to sodium dodecyl sulfate polyacrylamide gel electrophoresis and examined by immunoblot as previously described[76] or with modified blocking conditions where Odyssey blocking buffer (Li-Cor 927-40000; Li-Cor Biosciences, Lincoln, NE) replaced 5% milk, depending on the method of acquisition (enhanced chemiluminescence or Odyssey acquisition). Primary antibodies used were as follows: pAKT (Ser473) (Cell Signaling Technology; cat# 4060, 1:2000), AKT (Cell Signaling Technology; cat #9272, 1:1000), hepcidin (Abcam; cat# ab75883, 1:1000), Heme oxygenase (Abcam; cat# ab68477, 1:10 000)), p62 (Abcam; cat# ab56416, 1:1000), pCreb (Ser133) (Cell Signaling Technology 9198; 1:1000), Creb (Cell Signaling Technology 9104; 1:1000), MitoOxphos (Abcam; ab110413, 1:250), alpha-tubulin (Abcam; ab4074, 1:2500-5000 and Calbiochem, San Diego, CA; CP06 1:10000), Cyp4A (Abcam; ab3573, 1:1000), Cyp2E1 (Abcam; ab28146, 1:2500). Secondary antibodies used were IRDye (Li-Cor Biosciences) 680 or 800 (Li-Cor Biosciences; 1:10,000 to 1:20,000), and antibodies for enhanced chemiluminescence were goat anti-rabbit horseradish peroxidase (Bio-Rad; cat# 1721019, 1:5000). Signals were detected with Odyssey CLx (Li-Cor Biosciences) or by enhanced chemiluminescence (Pierce; cat# 32209). Results were normalized to total protein or tubulin.

Transmission Electron Microscopy

Electron microscopy was performed as previously described.[72] Briefly, P9 and P19 $Smn^{2B/+}$ and $Smn^{2B/-}$ mice were anesthetized and then perfused transcardially with 5

mL PBS, followed by 10–20 mL of Karnovsky's fixative (4% paraformaldehyde, 2% glutaraldehyde, and 0.1 mol/L sodium cacodylate in PBS, pH 7.4). Livers were collected and fixed overnight in the same fixative at 4°C. A liver segment of 1- to 2-mm length was collected from the same lobe of each mouse and processed for electron microscopy by a method previously described. All specimens were observed under a transmission electron microscope (Hitachi 7100, Gatan digital camera; Tokyo, Japan) operated at voltage 75 kV.

High-Resolution Respirometry and Mitochondrial Enzymatic Assays

These experiments were performed in Dr Harper's laboratory. Livers were excised from P9 and P19–21 $Smn^{2B/+}$ and $Smn^{2B/-}$ mice. Mitochondria were isolated using a slightly modified version previously described.[77] Briefly, livers were washed in IB_C buffer[77] and then minced and resuspended into 3 mL (P19) or 2 mL (P9) of IB_C buffer. Liver pieces were then transferred to a glass-Teflon homogenizer for homogenization using electric rotator. The homogenates were then centrifuged at $800g$ for 10 minutes at 4°C, and supernatant was transferred to a new tube and centrifuged again at $8600g$ for 10 minutes at 4°C, where pellet was resuspended in half initial volume of IB_C buffer. This process was repeated once. Mitochondria were indirectly quantified by Bradford assay. Seven hundred micrograms (P19–21) and 500 μg (P9) of mitochondria were then introduced in the high-resolution respirometer (O2K; Oroboros, Innsbruck, Austria) for respirometry measurements. The list and order of substrates and compounds introduced in the chamber for each protocol can be found in Supplementary Tables 2 and 3. The substrates and compounds were added to the chamber after mitochondria reached steady state. Quantification was performed using the Oroboros software.

CS and CPT1 Activity

These experiments were performed in Dr Harper's laboratory. Enzyme activity for CS and CPT1 was determined as previously described with some modifications.[78] Briefly, tissue was weighed and homogenized in ice-cold homogenization buffer (25 mmol/L Tris-HCL pH7.8, 1 mmol/L EDTA, 2 mmol/L $MgCL_2$, 50 mmol/L KCL, 0.50% Triton X-100) using modified Dounce homogenization with a pestle attached to a rotor. Homogenates were centrifuged at $14,000g$ for 10 minutes at 4°C, and the supernatant was collected. The assay was performed using the BioTek (Winooski, VT) Synergy 96-well microplate reading spectrophotometer at room temperature. CS activity was determined by measuring absorbance at 412 nm in 50 mmol/L Tris-HCl (pH 8.0) with 0.2 mmol/L DTNB, 0.1 mmol/L acetyl-coa, and 0.25 mmol/L oxaloacetate. Rate of absorbance change and path length of each well were determined using BioGen 5.0. The enzyme activities were calculated using the extinction factor, 13.6 mmol/L-1 cm-1 for CS. For CPT1 enzymatic assay, CPT1 activity was determined by measuring absorbance at 412 nm in 50 mmol/L Tris-HCl pH 8.0 with 0.2 mmol/L DTNB in a buffer containing 150 mmol/L KCl, 0.1 mmol/L palmitoyl-CoA, and 0.25 mmol/L l-carnitine. Enzymatic activity was reported as the activity per mg of tissue.

Lipid Quantification

Tissues were extracted and flash frozen. When required, tissues were pooled to obtain 100 mg. Tissue lipid analysis for quantification and profiles was performed at the Vanderbilt Mouse Metabolic Phenotyping Center. Briefly, lipids were extracted using the method of Folch-Lees.[79] The extracts were filtered, and lipids were recovered in the chloroform phase. Individual lipid classes were separated by thin layer chromatography using Silica Gel 60 A plates developed in petroleum ether, ethyl ether, acetic acid (80:20:1), and visualized by rhodamine 6G. Phospholipids, diglycerides, triglycerides, and cholesteryl esters were scraped from the plates and methylated using BF3/methanol as described previously.[80] The methylated fatty acids were extracted and analyzed by gas chromatography. Gas chromatographic analyses were performed on an Agilent 7890A gas chromatograph equipped with flame ionization detectors, a capillary column (SP2380, 0.25 mm × 30 m, 0.25 μm film; Supelco, Bellefonte, PA). Helium was used as a carrier gas. The oven temperature was programmed from 160°C to 230°C at 4°C/min. Fatty acid methyl esters were identified by comparing the retention times with those of known standards. Inclusion of lipid standards with odd chain fatty acids permitted quantification of the amount of lipid in the sample. Dipentadecanoyl phosphatidylcholine (C15:0), diheptadecanoin (C17:0), trieicosenoin (C20:1), and cholesteryl eicosenoate (C20:1) were used as standards.

Blood Chemistry

Blood was collected after decapitation of the mice and collection of the blood via capillary using Microcuvette CB 300 K2E coated with K2 EDTA (16.444.100). All the blood collected in this study was sampled randomly (ie, no fasting period) between 9 and 11 AM to limit the effect of the circadian rhythm. Mice were subsequently dissected as soon as possible to limit the effect of fasting. Samples were then spun at $2000g$ for 5 minutes at room temperature to extract plasma. Samples were pooled when large assay volume was required. Analysis of albumin, total protein, ALP, ALT, AST, bilirubin, iron, and NEFA (P19 only) was performed at the National Mouse Metabolic Phenotyping Center at the University of Massachusetts Medical School using a Cobas Clinical Chemistry Analyzer (Roche Diagnostics, Indianapolis, IN), and plasma NEFA levels were measured photometrically using a kit (Zenbio, Durham, NC), according to the manufacturer's protocol. Analysis of glucose, triglycerides, and NEFA (P9–P13) was performed at Comparative Clinical Pathology Services, LLC, Columbia, MO using commercially available assays on a Beckman-Coulter AU680 Automated Clinical Chemistry analyzer (Beckman-Coulter, Inc, Brea, CA). Triglyceride and glucose assays were obtained from Beckman-Coulter and the assay for nonessential fatty acids from Randox Laboratories (Kearneysville, WV). In this

study, we also used Luminex (Austin, TX) xMAP technology. The multiplexing analysis was performed using the Luminex 100 system by Eve Technologies Corp (Calgary, Alberta, Canada). Eleven markers were simultaneously measured in the samples using a MILLIPLEX Mouse Cytokine/Chemokine 11-plex kit (Millipore, St Charles, MO) according to the manufacturer's protocol. The 11-plex consisted of amylin (active), C-peptide 2, GIP (total), GLP-1 (active), ghrelin (active), glucagon, insulin, leptin, PP, PYY, and resistin. The assay sensitivies of these markers range from 1 to 23 pg/mL for the 11-plex. Individual analyte values are available in the MILLIPLEX protocol. IGF1 was measured in the samples using a R&D Systems Mouse 1-Plex Luminex Assay (R&D Systems, Minneapolis, MN) according to the manufacturer's protocol. The assay sensitivity of this marker is 3.46 pg/mL. Adiponectin was measured in the samples using MILLIPLEX Mouse Cytokine/Chemokine 1-plex kit (Millipore) according to the manufacturer's protocol. The assay sensitivity of this marker is 3 pg/mL. For experiments using Luminex system, if analytes were too low to be identified and outside of the dynamic range, it was deemed to be 0 and reflected as such on dot plot graphs.

Proteomic Analysis

Proteomic analysis was performed in Drs Parson's and Wishart's laboratories. Protein extraction, peptide TMT, and fractionation were performed by the FingerPrints Proteomics facilities at the University of Dundee. Protein samples were thawed, and proteins were extracted from each sample using Tris-HCl buffer (100 mmol/L, pH 8.5) containing 4% sodium dodecyl sulfate and 100 mmol/L dithiothreitol. Samples are then processed using FASP protocol[81] with some modifications. After removal of sodium dodecyl sulfate with 8 mol/L urea, proteins were alkylated with iodoacetamide, and filters were washed 3 times with 100 mmol/L Tris-HCL pH 8 and then twice with 100 mmol/L triethyl ammonium bicarbonate (TEAB). Proteins on the filters were then digested twice at 30°C with trypsin (2 × 2 μg), first overnight and then for another 6 hours in a final volume of 200 μL. Resulting tryptic peptides were desalted using C18 solid phase extraction cartridge (Empore; Agilent Technologies), dried, dissolved in 100 mmol/L TEAB, and quantified using Pierce Quantitative Colorimetric Peptide Assay (Thermo Scientific). One hundred micrograms of desalted tryptic peptides per sample was dissolved in 100 μL of 100 mmol/L TEAB. The 10 different TMT labels comprising the TMT10plex kit (Thermo Fisher Scientific) were dissolved in 41 μL anhydrous acetonitrile. Each dissolved label was added to a different sample. Samples were labelled as follows: sample B: Tag 127N Liver from 3 WT mice at P0; sample D: Tag 128N Liver from 3 $Smn^{2B/-}$ mice at P0; sample G: Tag 129C Liver from 3 WT mice at P2; sample I: Tag 130C Liver from 3 $Smn^{2B/-}$ mice at P2 (this was part of a wider proteomic screen, hence the discontinuous lettering). The sample-label mixture was incubated for 1 hour at room temperature. Labelling reaction was stopped by adding 8 μL of 5% hydroxylamine per sample. After labelling with TMT, samples were mixed, desalted, and dried in a speed-vac at

30°C. Samples were re-dissolved in 200 μL ammonium formate (NH_4HCO_2) (10 mmol/L, pH 10), and peptides were fractionated using an Ultimate 3000 RP-High pH High Performance Liquid Chromatography column (Thermo-Scientific) containing an XBridge C18 column (XBridge peptide BEH, 130Å, 3.5 μm, 2.1 × 150 mm) (Waters, Dublin, Ireland) with an XBridge guard column (XBridge, C18, 3.5 μm, 2.1 × 10 mm). Buffers A and B used for fractionation consist of (A) 10 mmol/L ammonium formate in MilliQ water and (B) 10 mmol/L ammonium formate with 90% acetonitrile, respectively. Before use, both buffers were adjusted to pH 10 with ammonia. Fractions were collected using a WPS-3000FC auto-sampler (Thermo-Scientific) at 1-minute intervals. Column and guard column were equilibrated with 2% Buffer B for 20 minutes at a constant flow rate of 0.2 mL/min. One hundred seventy-five microliters per sample was loaded onto the column at a rate of 0.2 mL/min, and the separation gradient was started 1 minute after sample was loaded onto the column. Peptides were eluted from the column with a gradient of 2% Buffer B to 5% Buffer B in 6 minutes and then from 5% Buffer B to 60% Buffer B in 50 minutes. Column was washed for 16 minutes in 100% Buffer B and equilibrated at 2% Buffer B for 20 minutes as mentioned previously. The fraction collection started 1 minute after injection and stopped after 80 minutes (total 80 fractions, 200 μL each). The total number of fractions concatenated was set to 15, and the content of the fractions was dried and suspended in 50 μL of 1% formic acid before analysis with liquid chromatography-mass spectrometry (LC-MS).

LC-MS/MS Analysis

Liquid chromatography-tandem mass spectrometry was performed by FingerPrints Proteomics Facilities at the University of Dundee to the following protocol. Analysis of peptide readout was performed on a Q Exactive HF Hybrid Quadrupole-Orbitrap Mass Spectrometer (Thermo Scientific) coupled with a Dionex Ultimate 3000 RS (Thermo Scientific). LC buffers were made up to the following: Buffer A (2% acetonitrile and 0.1% formic acid in Milli-Q water [v/v]) and Buffer B (80% acetonitrile and 0.08% formic acid in Milli-Q water [v/v]). Aliquots of 15 μL per sample were loaded at a rate of 5 μL/min onto a trap column (100 μm × 2 cm, PepMap nanoViper C18 column, 5 μm, 100 Å; Thermo Scientific) that was equilibrated with 98% Buffer A. The trap column was washed for 6 minutes at the same flow rate, and then the trap column was switched in-line with a resolving C18 column (Thermo Scientific) (75 μm × 50 cm, PepMap RSLC C18 column, 2 μm, 100 Å). Peptides were eluted from the column at a constant flow rate of 300 nL/min with a linear gradient from 95% Buffer A to 40% Buffer B in 122 minutes and then to 98% Buffer B by 132 minutes. The resolving column was then washed with 95% Buffer B for 15 minutes and re-equilibrated in 98% Buffer A for 32 minutes. Q Exactive HF was used in data dependent mode. A scan cycle was composed of a MS1 scan (m/z range from 335 to 1800, with a maximum ion injection time of 50 ms, a resolution of 120,000, and automatic gain control value of

3×10^6), followed by 15 sequential-dependent MS2 scans (with an isolation window set to 0.4 Da, resolution at 60,000, maximum ion injection time at 200 ms, and automatic gain control 1×10^5. To ensure mass accuracy, the mass spectrometer was calibrated on the first day that the runs were performed.

Database Search and Protein Identifications

Raw MS data from the 15 fractions were searched against mouse (*Mus musculus*) protein sequences from UniProtKB/Swiss-Prot (Version 20160629) using the MASCOT search engine (Matrix Science, Version 2.4) through Proteome Discoverer software (Version 1.4.1.14; Thermo Fisher). Parameters for database search were as follows: MS1 tolerance: 10 ppm; MS2 tolerance: 0.06 Da; fixed modification: carbamidomethyl (C) variable modification: oxidation (M), dioxidation (M), acetyl (N-term), Gln->pyro-Glu (N-term Q), TMT 10 (N-term and K); maximum missed cleavage 2; and target false discovery rate 0.01. All identifications were quantified as relative ratios of expression compared with control (WT at P0) through Proteome Discoverer software (Thermo Fisher; Version detailed above). Relative ratios along with UnitProtKB/Swiss-Prot identifications were exported into Microsoft Excel (Redmond, WA) as a raw data file for further in silico analysis.

In Silico Analysis

Mass spec data (from above) were manually subdivided into 4 distinct groups: Group A, (changed at P0 but not at P2); B (changed at P0 and P2); C (not changed at P0 but changed at P2); and NS, depending on the protein expression changes at P0 and P2 with level of significance identified as expression change increased or decreased by 20%. This procedure allows proteins most likely to be involved in the development of pathology, namely those altered at P0 and P2 or P2 only (Groups B and C), to be identified. These subgroups were then uploaded into the BioLayout *Express*3D for expression profile clustering, DAVID functional annotation for enrichment analysis, or IPA for hierarchical cascade mapping and upstream regulator prediction.

BioLayoutExpress3D

BioLayout*Express*3D[82] is a tool for visualization and clustering data. Routinely, proteomic data sets are uploaded to BioLayout *Express*3D, a Pearson's correlation coefficient (r value) is used to measure similarity between protein expression profiles, and a threshold for the Pearson's correlation coefficient is set. The data set is then visualized as nodes (proteins) that are connected to each other in a network based on their expression levels (edges). This data set can further be subdivided into discrete "clusters" based on a Markov Clustering Algorithm (MCL), thus segregating data in an unbiased manner as previously described.[83–85]

DAVID

DAVID provides a widely accepted set of functional annotation tools to interrogate the molecular composition of data sets relative to known findings in the current literature.[86,87] The functional clustering tool divides a list of proteins into functional protein groups, each with a different Enrichment Score, thus assigning a significance value. Where appropriate, analysis was carried out as previously described.[83,85]

Statistics

Data are presented as the mean $\pm$ standard error of the mean. A two-sided Student t test was performed using Microsoft Excel or GraphPad Prism 7 (San Diego, CA) to compare the means of data when only 2 groups were compared (ie, WT vs $Smn^{2B/-}$). One-way analysis of variance (ANOVA) and two-way ANOVA were also used to distinguish differences between more than 2 groups when multiple comparisons were necessary (ie, WT vs $Smn^{2B/+}$ vs $Smn^{2B/-}$) or additional variables were present. The post-test used for the analysis of variance was either Tukey or Sidak. Significance was set at $*P \leq .05$, $**P \leq .01$, $***P \leq .001$, and $****P \leq .0001$. Number for each experiment is as indicated in the figure legends.

Data and Materials Availability

All authors had access to the study data and had reviewed and approved the final manuscript. All data associated with this study are available in the main text or the supplementary materials. Raw data can be provided upon request.

References

1. Loomba R, Sanyal AJ. The global NAFLD epidemic. Nat Rev Gastroenterol Hepatol 2013;10:686–690.
2. Schwimmer JB, Deutsch R, Kahen T, Lavine JE, Stanley C, Behling C. Prevalence of fatty liver in children and adolescents. Pediatrics 2006;118:1388–1393.
3. Matteoni CA, Younossi ZM, Gramlich T, Boparai N, Liu YC, McCullough AJ. Nonalcoholic fatty liver disease: a spectrum of clinical and pathological severity. Gastroenterology 1999;116:1413–1419.
4. Adams LA, Lymp JF, St Sauver J, Sanderson SO, Lindor KD, Feldstein A, Angulo P. The natural history of nonalcoholic fatty liver disease: a population-based cohort study. Gastroenterology 2005;129:113–121.
5. Tandra S, Yeh MM, Brunt EM, Vuppalanchi R, Cummings OW, Unalp-Arida A, Wilson LA, Chalasani N. Presence and significance of microvesicular steatosis in nonalcoholic fatty liver disease. J Hepatol 2011; 55:654–659.
6. Hardy T, Oakley F, Anstee QM, Day CP. Nonalcoholic fatty liver disease: pathogenesis and disease spectrum. Annu Rev Pathol 2016;11:451–496.
7. Farrell GC, Larter CZ. Nonalcoholic fatty liver disease: from steatosis to cirrhosis. Hepatology 2006;43(Suppl 1): S99–S112.
8. Leoni S, Tovoli F, Napoli L, Serio I, Ferri S, Bolondi L. Current guidelines for the management of non-alcoholic fatty liver disease: a systematic review with comparative analysis. World J Gastroenterol 2018;24:3361–3373.

9. Jonscher KR, Bruce KD. Current models of fatty liver disease: new insights, therapeutic targets and interventions. Adv Exp Med Biol 2019;1134:33–58.

10. Lau JK, Zhang X, Yu J. Animal models of non-alcoholic fatty liver disease: current perspectives and recent advances. J Pathol 2017;241:36–44.

11. Ibrahim SH, Hirsova P, Malhi H, Gores GJ. Animal models of nonalcoholic steatohepatitis: eat, delete, and inflame. Dig Dis Sci 2016;61:1325–1336.

12. Van Herck MA, Vonghia L, Francque SM. Animal models of nonalcoholic fatty liver disease: a starter's guide. Nutrients 2017;9:1072.

13. Charlton M, Krishnan A, Viker K, Sanderson S, Cazanave S, McConico A, Masuoko H, Gores G. Fast food diet mouse: novel small animal model of NASH with ballooning, progressive fibrosis, and high physiological fidelity to the human condition. Am J Physiol Gastrointest Liver Physiol 2011;301:G825–G834.

14. Rinella ME, Green RM. The methionine-choline deficient dietary model of steatohepatitis does not exhibit insulin resistance. J Hepatol 2004;40:47–51.

15. Itagaki H, Shimizu K, Morikawa S, Ogawa K, Ezaki T. Morphological and functional characterization of non-alcoholic fatty liver disease induced by a methionine-choline-deficient diet in C57BL/6 mice. Int J Clin Exp Pathol 2013;6:2683–2696.

16. Sahai A, Malladi P, Pan X, Paul R, Melin-Aldana H, Green RM, Whitington PF. Obese and diabetic db/db mice develop marked liver fibrosis in a model of nonalcoholic steatohepatitis: role of short-form leptin receptors and osteopontin. Am J Physiol Gastrointest Liver Physiol 2004;287:G1035–G1043.

17. Bowerman M, Murray LM, Beauvais A, Pinheiro B, Kothary R. A critical smn threshold in mice dictates onset of an intermediate spinal muscular atrophy phenotype associated with a distinct neuromuscular junction pathology. Neuromuscular Disorders 2012;22:263–276.

18. Eshraghi M, McFall E, Gibeault S, Kothary R. Effect of genetic background on the phenotype of the Smn2B/- mouse model of spinal muscular atrophy. Hum Mol Genet 2016;25:4494–4506.

19. Deguise MO, De Repentigny Y, McFall E, Auclair N, Sad S, Kothary R. Immune dysregulation may contribute to disease pathogenesis in spinal muscular atrophy mice. Hum Mol Genet 2017;26:810–819.

20. Doktor TK, Hua Y, Andersen HS, Broner S, Liu YH, Wieckowska A, Dembic M, Bruun GH, Krainer AR, Andresen BS. RNA-sequencing of a mouse-model of spinal muscular atrophy reveals tissue-wide changes in splicing of U12-dependent introns. Nucleic Acids Res 2017;45:395–416.

21. So BR, Zhang Z, Dreyfuss G. The function of survival motor neuron complex and its role in spinal muscular atrophy pathogenesis. In: Sumner CJ, Paushkin S, Ko CP, eds. Spinal muscular atrophy: disease mechanisms and therapy. New York: Elsevier, 2016:99–111.

22. Zhang Z, Lotti F, Dittmar K, Younis I, Wan L, Kasim M, Dreyfuss G. SMN deficiency causes tissue-specific perturbations in the repertoire of snRNAs and widespread defects in splicing. Cell 2008;133:585–600.

23. Tisdale S, Pellizzoni L. RNA-processing dysfunction in spinal muscular atrophy. In: Sumner CJ, Paushkin S, Ko CP, eds. Spinal muscular atrophy: disease mechanisms and therapy. New York: Elsevier, 2017:75–97.

24. Deguise MO, Baranello G, Mastella C, Beauvais A, Michaud J, Leone A, De Amicis R, Battezzati A, Dunham C, Selby K, Warman Chardon J, McMillan HJ, Huang YT, Courtney NL, Mole AJ, Kubinski S, Claus P, Murray LM, Bowerman M, Gillingwater TH, Bertoli S, Parson SH, Kothary R. Abnormal fatty acid metabolism is a core component of spinal muscular atrophy. Ann Clin Transl Neurol 2019;6:1519–1532.

25. McMillan HJ, Gregas M, Darras BT, Kang PB. Serum transaminase levels in boys with Duchenne and Becker muscular dystrophy. Pediatrics 2011;127:e132–e136.

26. Boyer JG, Deguise MO, Murray LM, Yazdani A, De Repentigny Y, Boudreau-Lariviere C, Kothary R. Myogenic program dysregulation is contributory to disease pathogenesis in spinal muscular atrophy. Hum Mol Genet 2014;23:4249–4259.

27. Shu KX, Li B, Wu LX. The p53 network: p53 and its downstream genes. Colloids Surf B Biointerfaces 2007; 55:10–18.

28. Lee YA, Wallace MC, Friedman SL. Pathobiology of liver fibrosis: a translational success story. Gut 2015; 64:830–841.

29. Nishizawa H, Iguchi G, Fukuoka H, Takahashi M, Suda K, Bando H, Matsumoto R, Yoshida K, Odake Y, Ogawa W, Takahashi Y. IGF-I induces senescence of hepatic stellate cells and limits fibrosis in a p53-dependent manner. Sci Rep 2016;6:34605.

30. Nishikawa T, Bell A, Brooks JM, Setoyama K, Melis M, Han B, Fukumitsu K, Handa K, Tian J, Kaestner KH, Vodovotz Y, Locker J, Soto-Gutierrez A, Fox IJ. Resetting the transcription factor network reverses terminal chronic hepatic failure. J Clin Invest 2015; 125:1533–1544.

31. Guzman-Lepe J, Cervantes-Alvarez E, Collin de l'Hortet A, Wang Y, Mars WM, Oda Y, Bekki Y, Shimokawa M, Wang H, Yoshizumi T, Maehara Y, Bell A, Fox IJ, Takeishi K, Soto-Gutierrez A. Liver-enriched transcription factor expression relates to chronic hepatic failure in humans. Hepatol Commun 2018;2:582–594.

32. Britton LJ, Subramaniam VN, Crawford DH. Iron and non-alcoholic fatty liver disease. World J Gastroenterol 2016;22:8112–8122.

33. Evstatiev R, Gasche C. Iron sensing and signalling. Gut 2012;61:933–952.

34. Szunyogova E, Zhou H, Maxwell GK, Powis RA, Francesco M, Gillingwater TH, Parson SH. Survival motor neuron (SMN) protein is required for normal mouse liver development. Sci Rep 2016;6:34635.

35. Vitte JMM, Davoult B, Roblot N, Mayer M, Joshi V, Courageot S, Tronche F, Vadrot J, Moreau MH, Kemeny F, Melki J. Deletion of murine Smn exon 7 directed to liver leads to severe defect of liver development associated with iron overload. Am J Pathol 2004; 165:1731–1741.

36. Hua Y, Sahashi K, Rigo F, Hung G, Horev G, Bennett CF, Krainer AR. Peripheral SMN restoration is essential for

long-term rescue of a severe spinal muscular atrophy mouse model. Nature 2011;478:123–126.

37. Sahashi K, Ling KK, Hua Y, Wilkinson JE, Nomakuchi T, Rigo F, Hung G, Xu D, Jiang Y-PP, Lin RZ, Ko C-PP, Bennett CF, Krainer AR. Pathological impact of SMN2 mis-splicing in adult SMA mice. EMBO Mol Med 2013; 5:1586–1601.

38. Murdocca M, Malgieri A, Luchetti A, Saieva L, Dobrowolny G, de Leonibus E, Filareto A, Quitadamo MC, Novelli G, Musaro A, Sangiuolo F. IPLEX administration improves motor neuron survival and ameliorates motor functions in a severe mouse model of spinal muscular atrophy. Mol Med 2012;18:1076–1085.

39. Yao Y, Miao X, Zhu D, Li D, Zhang Y, Song C, Liu K. Insulin-like growth factor-1 and non-alcoholic fatty liver disease: a systemic review and meta-analysis. Endocrine 2019;65:227–237.

40. Larsen S, Nielsen J, Hansen CN, Nielsen LB, Wibrand F, Stride N, Schroder HD, Boushel R, Helge JW, Dela F, Hey-Mogensen M. Biomarkers of mitochondrial content in skeletal muscle of healthy young human subjects. J Physiol 2012;590:3349–3360.

41. Bjorkoy G, Lamark T, Pankiv S, Overvatn A, Brech A, Johansen T. Monitoring autophagic degradation of p62/SQSTM1. Methods Enzymol 2009;452:181–197.

42. Rutkowski DT, Wu J, Back SH, Callaghan MU, Ferris SP, Iqbal J, Clark R, Miao H, Hassler JR, Fornek J, Katze MG, Hussain MM, Song B, Swathirajan J, Wang J, Yau GD, Kaufman RJ. UPR pathways combine to prevent hepatic steatosis caused by ER stress-mediated suppression of transcriptional master regulators. Dev Cell 2008; 15:829–840.

43. Gonzalez-Rodriguez A, Mayoral R, Agra N, Valdecantos MP, Pardo V, Miquilena-Colina ME, Vargas-Castrillon J, Lo Iacono O, Corazzari M, Fimia GM, Piacentini M, Muntane J, Bosca L, Garcia-Monzon C, Martin-Sanz P, Valverde AM. Impaired autophagic flux is associated with increased endoplasmic reticulum stress during the development of NAFLD. Cell Death Dis 2014; 5:e1179.

44. Hardwick JP, Osei-Hyiaman D, Wiland H, Abdelmegeed MA, Song BJ. PPAR/RXR regulation of fatty acid metabolism and fatty acid omega-hydroxylase (CYP4) isozymes: implications for prevention of lipotoxicity in fatty liver disease. PPAR Res 2009; 2009:952734.

45. Berlanga A, Guiu-Jurado E, Porras JA, Auguet T. Molecular pathways in non-alcoholic fatty liver disease. Clin Exp Gastroenterol 2014;7:221–239.

46. Bowerman M, Swoboda KJ, Michalski J-PP, Wang G-SS, Reeks C, Beauvais A, Murphy K, Woulfe J, Screaton RA, Scott FW, Kothary R. Glucose metabolism and pancreatic defects in spinal muscular atrophy. Ann Neurol 2012;72:256–268.

47. Yakar S, Setser J, Zhao H, Stannard B, Haluzik M, Glatt V, Bouxsein ML, Kopchick JJ, LeRoith D. Inhibition of growth hormone action improves insulin sensitivity in liver IGF-1-deficient mice. J Clin Invest 2004; 113:96–105.

48. Herzig S, Long F, Jhala US, Hedrick S, Quinn R, Bauer A, Rudolph D, Schutz G, Yoon C, Puigserver P, Spiegelman B, Montminy M. CREB regulates hepatic gluconeogenesis through the coactivator PGC-1. Nature 2001;413:179–183.

49. Campbell JE, Drucker DJ. Islet alpha cells and glucagon: critical regulators of energy homeostasis. Nat Rev Endocrinol 2015;11:329–338.

50. Perseghin G, Lattuada G, De Cobelli F, Ragogna F, Ntali G, Esposito A, Belloni E, Canu T, Terruzzi I, Scifo P, Del Maschio A, Luzi L. Habitual physical activity is associated with intrahepatic fat content in humans. Diabetes Care 2007;30:683–688.

51. Gauthier MS, Couturier K, Latour JG, Lavoie JM. Concurrent exercise prevents high-fat-diet-induced macrovesicular hepatic steatosis. J Appl Physiol 2003; 94:2127–2134.

52. Tetri LH, Basaranoglu M, Brunt EM, Yerian LM, Neuschwander-Tetri BA. Severe NAFLD with hepatic necroinflammatory changes in mice fed trans fats and a high-fructose corn syrup equivalent. Am J Physiol Gastrointest Liver Physiol 2008;295:G987–G995.

53. Ito M, Suzuki J, Tsujioka S, Sasaki M, Gomori A, Shirakura T, Hirose H, Ito M, Ishihara A, Iwaasa H, Kanatani A. Longitudinal analysis of murine steatohepatitis model induced by chronic exposure to high-fat diet. Hepatol Res 2007;37:50–57.

54. Deguise MO, Chehade L, Tierney A, Beauvais A, Kothary R. Low fat diets increase survival of a mouse model of spinal muscular atrophy. Ann Clin Transl Neurol 2019;6:2340–2346.

55. Marin V, Rosso N, Dal Ben M, Raseni A, Boschelle M, Degrassi C, Nemeckova I, Nachtigal P, Avellini C, Tiribelli C, Gazzin S. An animal model for the juvenile non-alcoholic fatty liver disease and non-alcoholic steatohepatitis. PLoS One 2016;11:e0158817.

56. Fu JF, Fang YL, Liang L, Wang CL, Hong F, Dong GP. A rabbit model of pediatric nonalcoholic steatohepatitis: the role of adiponectin. World J Gastroenterol 2009; 15:912–918.

57. Fan CY, Pan J, Chu R, Lee D, Kluckman KD, Usuda N, Singh I, Yeldandi AV, Rao MS, Maeda N, Reddy JK. Hepatocellular and hepatic peroxisomal alterations in mice with a disrupted peroxisomal fatty acyl-coenzyme A oxidase gene. J Biol Chem 1996; 271:24698–24710.

58. Schuppan D, Afdhal NH. Liver cirrhosis. Lancet 2008; 371:838–851.

59. Dal K, Bulur O, Ata N, Yeniova AO, Baser S, Karakaya S, Unsal O, Dagdeviren M, Karadag I, Beyan E, Ertugrul DT. The role of insulin - like growth factor - 1 on steatohepatitis. Acta Gastroenterol Belg 2017;80:21–24.

60. Adamek A, Kasprzak A. Insulin-like growth factor (IGF) system in liver diseases. Int J Mol Sci 2018;19(5).

61. Allard JB, Duan C. IGF-binding proteins: why do they exist and why are there so many? Front Endocrinol (Lausanne) 2018;9:117.

62. Hegarty R, Deheragoda M, Fitzpatrick E, Dhawan A. Paediatric fatty liver disease (PeFLD): all is not

NAFLD—pathophysiological insights and approach to management. J Hepatol 2018;68:1286–1299.

63. Murray LM, Beauvais A, Gibeault S, Courtney NL, Kothary R. Transcriptional profiling of differentially vulnerable motor neurons at pre-symptomatic stage in the Smn (2b/-) mouse model of spinal muscular atrophy. Acta Neuropathol Commun 2015;3:55.

64. Neve A, Trüb J, Saxena S, Schümperli D. Central and peripheral defects in motor units of the diaphragm of spinal muscular atrophy mice. Mol Cell Neurosci 2016;70:30–41.

65. Wishart TM, Mutsaers CA, Riessland M, Reimer MM, Hunter G, Hannam ML, Eaton SL, Fuller HR, Roche SL, Somers E, Morse R, Young PJ, Lamont DJ, Hammerschmidt M, Joshi A, Hohenstein P, Morris GE, Parson SH, Skehel PA, Becker T, Robinson IM, Becker CG, Wirth B, Gillingwater TH. Dysregulation of ubiquitin homeostasis and β-catenin signaling promote spinal muscular atrophy. J Clin Invest 2014;124:1821–1834.

66. Miller N, Shi H, Zelikovich AS, Ma YC. Motor neuron mitochondrial dysfunction in spinal muscular atrophy. Hum Mol Genet 2016;25:3395–3406.

67. Fuller HR, Mandefro B, Shirran SL, Gross AR, Kaus AS, Botting CH, Morris GE, Sareen D. Spinal muscular atrophy patient iPSC-derived motor neurons have reduced expression of proteins important in neuronal development. Front Cell Neurosci 2015;9:506.

68. Boyd PJ, Tu WY, Shorrock HK, Groen EJN, Carter RN, Powis RA, Thomson SR, Thomson D, Graham LC, Motyl AAL, Wishart TM, Highley JR, Morton NM, Becker T, Becker CG, Heath PR, Gillingwater TH. Bioenergetic status modulates motor neuron vulnerability and pathogenesis in a zebrafish model of spinal muscular atrophy. PLoS Genet 2017;13:e1006744.

69. Acsadi G, Lee I, Li X, Khaidakov M, Pecinova A, Parker GC, Huttemann M. Mitochondrial dysfunction in a neural cell model of spinal muscular atrophy. J Neurosci Res 2009;87:2748–2756.

70. Berger A, Mayr JA, Meierhofer D, Fotschl U, Bittner R, Budka H, Grethen C, Huemer M, Kofler B, Sperl W. Severe depletion of mitochondrial DNA in spinal muscular atrophy. Acta Neuropathol 2003;105:245–251.

71. Ripolone M, Ronchi D, Violano R, Vallejo D, Fagiolari G, Barca E, Lucchini V, Colombo I, Villa L, Berardinelli A, Balottin U, Morandi L, Mora M, Bordoni A, Fortunato F, Corti S, Parisi D, Toscano A, Sciacco M, DiMauro S, Comi GP, Moggio M. Impaired muscle mitochondrial biogenesis and myogenesis in spinal muscular atrophy. JAMA Neurol 2015;72:666–675.

72. Deguise M, Boyer JG, McFall ER, Yazdani A, De Repentigny Y, Kothary R. Differential induction of muscle atrophy pathways in two mouse models of spinal muscular atrophy. Sci Rep 2016;6:28846.

73. Foust KD, Wang X, McGovern VL, Braun L, Bevan AK, Haidet AM, Le TT, Morales PR, Rich MM, Burghes AH, Kaspar BK. Rescue of the spinal muscular atrophy

74. D'Costa S, Blouin V, Broucque F, Penaud-Budloo M, Francois A, Perez IC, Le Bec C, Moullier P, Snyder RO, Ayuso E. Practical utilization of recombinant AAV vector reference standards: focus on vector genomes titration by free ITR qPCR. Mol Ther Methods Clin Dev 2016;5:16019.

75. Zhang Z, Zhang F, An P, Guo X, Shen Y, Tao Y, Wu Q, Zhang Y, Yu Y, Ning B, Nie G, Knutson MD, Anderson GJ, Wang F. Ferroportin1 deficiency in mouse macrophages impairs iron homeostasis and inflammatory responses. Blood 2011;118:1912–1922.

76. Shafey D, Boyer JG, Bhanot K, Kothary R. Identification of novel interacting protein partners of SMN using tandem affinity purification. J Proteome Res 2010;9:1659–1669.

77. Frezza C, Cipolat S, Scorrano L. Organelle isolation: functional mitochondria from mouse liver, muscle and cultured fibroblasts. Nat Protoc 2007;2:287–295.

78. Pileggi CA, Hedges CP, Segovia SA, Markworth JF, Durainayagam BR, Gray C, Zhang XD, Barnett MP, Vickers MH, Hickey AJ, Reynolds CM, Cameron-Smith D. Maternal high fat diet alters skeletal muscle mitochondrial catalytic activity in adult male rat offspring. Front Physiol 2016;7:546.

79. Folch J, Lees M, Sloane Stanley GH. A simple method for the isolation and purification of total lipides from animal tissues. J Biol Chem 1957;226:497–509.

80. Morrison WR, Smith LM. Preparation of fatty acid methyl esters and dimethylacetals from lipids with boron fluoride–methanol. J Lipid Res 1964;5:600–608.

81. Wisniewski JR, Zougman A, Nagaraj N, Mann M. Universal sample preparation method for proteome analysis. Nat Methods 2009;6:359–362.

82. Theocharidis A, van Dongen S, Enright AJ, Freeman TC. Network visualization and analysis of gene expression data using BioLayout Express(3D). Nat Protoc 2009;4:1535–1550.

83. Graham LC, Eaton SL, Brunton PJ, Atrih A, Smith C, Lamont DJ, Gillingwater TH, Pennetta G, Skehel P, Wishart TM. Proteomic profiling of neuronal mitochondria reveals modulators of synaptic architecture. Mol Neurodegener 2017;12:77.

84. Jones RA, Harrison C, Eaton SL, Llavero Hurtado M, Graham LC, Alkhammash L, Oladiran OA, Gale A, Lamont DJ, Simpson H, Simmen MW, Soeller C, Wishart TM, Gillingwater TH. Cellular and molecular anatomy of the human neuromuscular junction. Cell Rep 2017;21:2348–2356.

85. Llavero Hurtado M, Fuller HR, Wong AMS, Eaton SL, Gillingwater TH, Pennetta G, Cooper JD, Wishart TM. Proteomic mapping of differentially vulnerable presynaptic populations identifies regulators of neuronal stability in vivo. Sci Rep 2017;7:12412.

86. Huang da W, Sherman BT, Lempicki RA. Systematic and integrative analysis of large gene lists using

DAVID bioinformatics resources. Nat Protoc 2009; 4:44–57.

87. Huang da W, Sherman BT, Lempicki RA. Bioinformatics enrichment tools: paths toward the comprehensive functional analysis of large gene lists. Nucleic Acids Res 2009;37:1–13.

Correspondence
Address correspondence to: Rashmi Kothary, PhD, Ottawa Hospital Research Institute, 501 Smyth Road, Ottawa, Ontario, Canada K1H 8L6. e-mail: rkothary@ohri.ca; fax: (613) 737-8803.

CrediT Authorship Contributions
Marc-Olivier Deguise, MD, PhD (Conceptualization: Lead; Data curation: Lead; Formal analysis: Lead; Investigation: Lead; Methodology: Lead; Project administration: Supporting; Supervision: Supporting; Validation: Lead; Visualization: Lead; Writing – original draft: Lead; Writing – review & editing: Equal)

Chantal Pileggi, PhD (Conceptualization: Supporting; Data curation: Supporting; Formal analysis: Supporting; Investigation: Supporting; Methodology: Supporting; Resources: Supporting; Validation: Supporting; Writing – review & editing: Supporting)

Yves De Repentigny, MSc (Data curation: Supporting; Formal analysis: Supporting; Investigation: Supporting; Methodology: Supporting; Writing – review & editing: Supporting)

Ariane Beauvais, MSc (Data curation: Supporting; Formal analysis: Supporting; Methodology: Supporting)

Alexandra Tierney, BSc (Data curation: Supporting; Formal analysis: Supporting; Investigation: Supporting)

Lucia Chehade, BSc (Data curation: Supporting; Formal analysis: Supporting; Investigation: Supporting)

Jean Michaud, MD (Formal analysis: Supporting; Writing – review & editing: Supporting)

Maica Llavero-Hurtado, MPharm, PhD (Conceptualization: Supporting; Data curation: Supporting; Formal analysis: Supporting)

Douglas Lamont, BSc (Conceptualization: Supporting; Data curation: Supporting; Formal analysis: Supporting)

Abdelmadjid Atrih, PhD (Conceptualization: Supporting; Data curation: Supporting; Formal analysis: Supporting; Investigation: Supporting; Methodology: Supporting; Writing – review & editing: Supporting)

Thomas M. Wishart, PhD (Conceptualization: Supporting; Data curation: Supporting; Formal analysis: Supporting; Funding acquisition: Supporting; Investigation: Supporting; Project administration: Supporting; Writing – review & editing: Supporting)

Thomas H. Gillingwater, MBA, PhD (Conceptualization: Supporting; Data curation: Supporting; Formal analysis: Supporting; Funding acquisition: Supporting; Investigation: Supporting; Project administration: Supporting; Resources: Supporting; Supervision: Supporting; Writing – review & editing: Supporting)

Bernard L. Schneider, PhD (Funding acquisition: Supporting; Project administration: Supporting; Resources: Supporting; Writing – review & editing: Supporting)

Mary-Ellen Harper, PhD (Conceptualization: Supporting; Data curation: Supporting; Formal analysis: Supporting; Funding acquisition: Supporting; Investigation: Supporting; Methodology: Supporting; Project administration: Supporting; Supervision: Supporting; Writing – review & editing: Supporting)

Simon H. Parson, PhD (Conceptualization: Supporting; Data curation: Supporting; Formal analysis: Supporting; Funding acquisition: Supporting; Investigation: Supporting; Methodology: Supporting; Project administration: Supporting; Resources: Supporting; Supervision: Supporting; Writing – review & editing: Supporting)

Rashmi Kothary, PhD (Conceptualization: Equal; Funding acquisition: Lead; Project administration: Lead; Resources: Lead; Supervision: Lead; Writing – review & editing: Equal)

Supplementary Table 1. Primers Used in This Study

Gene name	Short form	Forward	Reverse	PrimePCR
TNF receptor superfamily member 6	FasR	TGTGAACATGGAACCCTTGA	TTCAGGGTCATCCTGTCTCC	
TNF receptor superfamily member 1A	TNFR1	CCGGGAGAAGAGGGATAGCTT	TCGGACAGTCACTCACCAAGT	
Caspase 8	Casp8	GGCCTCCATCTATGACCTGA	TGTGGTTCTGTTGCTCGAAG	
BCL2 associated X, apoptosis regulator	Bax	TGCAGAGGATGATTGCTGAC	GATCAGCTCGGGCACTTTAG	
BH3 interacting domain death agonist	Bid			qMmuCID0022679
Tumor protein P53	p53	GCTTCTCCGAAGACTGGATG	CTTCACTTGGGCCTTCAAAA	
Cyclin-dependent kinase inhibitor 1A (P21)	p21			qMmuCED0046265
Transformed mouse 3T3 cell double minute 2	Mdm2			qMmuCID0025320
Complement C1r	C1R	AACCATATTACAAGATGCTGACCA	CCTTGGGCTGTGCAGGTA	
Complement C1s	C1S	GGTGGATACTTCTGCTCCTGTC	AGGGCAGTGAACACATCTCC	
Complement C1q B chain	C1qb	CGTCGGCCCTAAGGGTACT	GGGGCTGTTGATGGTCCTC	
Complement C3	C3	CCAGCTCCCCATTAGCTCTG	GCACTTGCCTCTTTAGGAAGTC	
Complement C4	C4	TCTCACAAACCCCTCGACAT	AGCATCCTGGAACACCTGAA	
Complement C5	C5	AGGGTACTTTGCCTGCTGAA	TGTGAAGGTGCTCTTGGATG	
Complement C6	C6			qMmuCID0025195
Complement factor B	Factor B	GAGCGCAACTCCAGTGCTT	GAGGGACATAGGTACTCCAGG	
Coagulation factor II, thrombin	F2			qMmuCED0046327
Coagulation factor V	F5	CATGGAAACCTTACCGACAGAAA	CATGTGCCCCTTGGTATTGC	
Coagulation factor VII	F7	CGTCTGCTTCTGCCTCTTAGA	ATTTGCACAGATCAGCTGCTCAT	
Coagulation factor IX	F9	GCAAAACCGGGTCAAATCC	ACCTCCACAGAATGCCTCAATT	
Coagulation factor X	F10			qMmuCED0048020
Protein C, inactivator of coagulation factors Va and VIIIa	ProC			
Protein S	ProS			qMmuCED0045958
Protein Z, vitamin K dependent plasma glycoprotein	ProZ			
Thrombopoietin	Thpo			qMmuCED0037967
Hepatocyte nuclear factor 4 alpha	Hnf4a	AGAGGTTCTGTCCCAGCAGATC	CGTCTGTGATGTTGGCAATC	
Insulin-like growth factor 1	IGF1			qMmuCID0005726
Insulin-like growth factor 1 receptor	IGF1R			qMmuCID0005315
Insulin-like growth factor binding protein, acid labile subunit	IGFals			qMmuCID0008201
Insulin-like growth factor binding protein 1	IGFbp1			qMmuCID0027402
Insulin-like growth factor binding protein 3	IGFbp3			qMmuCID0005232
Hepcidin	Hamp	CCTATCTCCATCAACAGATG	AACAGATACCACACTGGGAA	
Transferrin	TF	CCATCCCATCACAACAAGGTATC	GCTAGTGTCCGATGCCTTCAC	
Heme oxygenase	Hmox1	GCCACCAAGGAGGTACACAT	GCTTGTTGCGCTCTATCTCC	
Ceruloplasmin	Cp	TCTACCAAGGAGTAGCCAGGA	ATCTTCCCTCTCATCCGTGC	
Ferritin light chain	L-Ferritin	CGTCTCCTCGAGTTTCAGAAC	CTCCTGGGTTTTACCCCATTC	

Supplementary Table 1. Continued

Gene name	Short form	Forward	Reverse	PrimePCR
Ferritin heavy chain	H-Ferritin	CCATCAACCGCCAGATCAAC	GCCACATCATCTCGGTCAAA	
Solute carrier family 40 member 1	Ferroportin	GCTGCTAGAATCGGTCTTTGGT	CAGCAACTGTGTCACCGTCAA	
Solute carrier family 11 (proton-coupled divalent metal ion transporters), member 2	Nramp2			qMmuCID0016356
Tyrosine 3-mono-oxygenase/ tryptophan 5-mono-oxygenase activation protein, zeta polypeptide	Ywhaz	AAGACAGCACGCTAATAATGC	TTGGAAGGCCGGTTAATTTTC	
Succinate dehydrogenase complex, subunit A, flavoprotein	Sdha	GCCTGGTCTGTATGCCTGTG	CCGATTCTTCTCCAGCATTTG	
Polymerase (RNA) II (DNA directed) polypeptide J	Polr2j	ACCACACTCTGGGGAACATC	CTCGCTGATGAGGTCTGTGA	
Hypoxanthine guanine phosphoribosyl transferase	Hprt1	CCCAGCGTCGTGATTAGTGATG	TTCAGTCCTGTCCATAATCAGTC	
Activation transcription factor 4	ATF4	GTTTGACTTCGATGCTCTGTTTC	GGGCTCCTTATTAGTCTCTTGG	
Binding-immunoglobulin protein	Bip	TTCAGCCAATTATCAGCAAACTCT	TTTTCTGATGTATCCTCTTCACCAGT	
94 kDa glucose-regulated protein	GRP94	AAGAATGAAGGAAAAACAGGACAAAA	CAAATGGAGAAGATTCCGCC	
C/EBP homologous protein	CHOP	CTGGAAGCCTGGTATGAGGAT	CAGGGTCAAGAGTAGTGAAGGT	

Supplementary Table 2. Oxygraph Protocol in the Absence of Fatty Acids

Substrate	Volume (μL)	Concentration of stock	Concentration of substrate in the chamber
Amplex ultra red	2	10 mmol/L	50 μmol/L
Horseradish peroxidase	10	10 mmol/L	10 U/mL
H2O2	5	40 μmol/L	0.1 μmol/L titrations $\times$ 3
800 mmol/L malate	5	800 mmol/L	2 mmol/L
Pyruvate	10	2 mol/L	5 mmol/L
ADP/Mg2+	20, 20	500 mmol/L	5 mmol/L
Glutamate	10	2 mol/L	10 mmol/L
Succinate	20	1 mol/L	10 mmol/L
500 mmol/L ADP/Mg	20, 20	500 mmol/L	5 mmol/L
Oligomycin	1	5 mmol/L	2.5 μmol/L
FCCP	0.5 μL titrations until maximum respiration	1 mmol/L	0.25 μmol/L titration
Antimycin A	1	5 mmol/L	2.5 μmol/L
Ascorbate + TMPD	5, 5	800 mmol/L Asc, 200 mmol/L TMPD	2 mmol/L Asc, 0.5 mmol/L TMPD
Sodium azide	50	4 mol/L	100 mmol/L

Supplementary Table 3. Oxygraph Protocol in the Presence of Fatty Acids

Substrate	Volume (μL)	Concentration of stock	Concentration of substrate in the chamber
800 mmol/L malate	5	800 mmol/L	2 mmol/L
Oct Car	4	100 mmol/L	0.2 mmol/L
ADP/Mg2+	20, 20	500 mmol/L	5 mmol/L
Pyruvate	10	2 mol/L	5 mmol/L
Glutamate	10	2 mol/L	10 mmol/L
Succinate	20	1 mol/L	10 mmol/L
500 mmol/L ADP/Mg	20, 20	500 mmol/L	5 mmol/L
Oligomycin	1	5 mmol/L	2.5 μmol/L
FCCP	0.5 μL titrations until maximum respiration	1 mmol/L	0.25 μmol/L titration
Antimycin A	1	5 mmol/L	2.5 μmol/L
Ascorbate + TMPD	5, 5	800 mmol/L Asc, 200 mmol/L TMPD	2 mmol/L Asc, 0.5 mmol/L TMPD
Sodium azide	50	4 mol/L	100 mmol/L